

# Micromechanical modeling and simulation of the loading path dependence of ductile failure by void growth to coalescence

Vishal Vishwakarma, Shyam M. Keralavarma\*

Department of Aerospace Engineering, Indian Institute of Technology Madras, Chennai 600036, India



## ARTICLE INFO

### Article history:

Received 27 November 2018

Revised 18 February 2019

Available online 22 February 2019

### Keywords:

Fracture mechanisms

Ductile failure

Void growth

Void coalescence

## ABSTRACT

The loading path dependence of ductile failure by void growth to coalescence is studied using a unit cell model of a porous material, containing a periodic distribution of voids in an elasto-plastic power law hardening matrix. The unit cell is subjected to triaxial proportional loading paths, and predictions for the strains to failure, defined as the onset of void coalescence by plastic strain localization in the inter-void ligaments, are obtained as a function of the loading path parameters, the stress triaxiality and the Lode parameter. Analogous simulations of a macroscopic material element subjected to proportional loading are performed using a multi-surface plasticity model, which accounts for void growth by diffuse plastic flow and void coalescence by the localization of plastic strains inside a micro-scale representative volume element. A phenomenological hardening law that approximately accounts for the physics of strain hardening during both pre- and post-coalescence deformation is proposed. The strains to failure in the continuum simulations are determined as the equivalent strains to the onset of void coalescence at the micro-scale of the voids. It is shown that the multi-surface plasticity model quantitatively predicts the loading path dependence of the strains to failure obtained from the cell model simulations over a wide range of values of the Lode parameter, from axisymmetric to shear dominated states, and moderate to large values of the stress triaxiality. Quantitative agreement with cell model simulations is obtained for two representative values of the strain hardening exponent, and in the absence of heuristic adjustable parameters in the model.

© 2019 Elsevier Ltd. All rights reserved.

## 1. Introduction

The growth and coalescence of micro-voids is a key mechanism of failure in ductile materials. The growth of micro-voids leads to material softening and promotes the onset of plastic instabilities such as necking or shear banding. The formation of such localization zones is quickly followed by crack nucleation and growth, aided by rapid void growth in the crack-tip process zones, leading to complete failure. Given that the void growth process is a result of plastic deformation of the matrix material, the damage growth rates are expected to be strongly influenced by the loading history. The loading path in stress space is usually characterized by two non-dimensional quantities, namely the stress triaxiality,  $T$ , and the Lode parameter,  $L$ , which are related to the ratios of the stress invariants. The triaxiality  $T$  is the ratio of the mean stress and the von Mises equivalent stress, while the Lode parameter is related to the determinant of the stress deviator normalized by the Mises

stress. It has long been established that the triaxiality plays a critical role in the damage growth process, which is a consequence of the hydrostatic stress dependence of void growth. As is well known from notched bar tension experiments (Hancock and MacKenzie, 1976; Hancock and Brown, 1983), the ductility decreases exponentially as a function of the stress triaxiality. However, the effect of the Lode parameter, which allows to distinguish between axisymmetric and shear dominated stress states for a given hydrostatic stress, on the ductility has historically received less attention in the literature.

The Lode parameter dependence of ductile failure has been brought into focus by several recent experimental studies aimed at understanding the mechanisms of failure under low triaxiality shear dominated loading conditions, when void growth is slow due to the low hydrostatic stress levels (Bao and Wierzbicki, 2004; Barsoum and Faleskog, 2007; Dunand and Mohr, 2011; Haltom et al., 2013; Papisidero et al., 2015). Bao and Wierzbicki (2004) used a series of fracture specimens, including notched bars, butterfly shear specimens and uniaxial compression pins to study ductile fracture over a wide range of average triaxialities ranging from positive to negative values. In contrast with the earlier studies of

\* Corresponding author.

E-mail address: [shyam@iitm.ac.in](mailto:shyam@iitm.ac.in) (S.M. Keralavarma).

Hancock and MacKenzie (1976), they reported a non-monotonic variation of the ductility as a function of the average triaxiality in their experiments, with the ductility increasing with decreasing triaxiality till a values of  $T \approx 0.4$  followed by a decrease in ductility towards lower values of  $T$ . Similar results were also reported by Barsoum and Faleskog (2007) using tension-torsion experiments on weldox steel specimens. However, Haltom et al. (2013) reported that the same trends could not be reproduced in tension-torsion experiments using Aluminum 6061 specimens. Many authors have suggested that the reduced ductility at low triaxialities observed in some experiments is a result of a change in failure mechanism at the micro-scale of the voids, from void growth to coalescence under highly triaxial stress states to shear strain localization between the voids (the so called void sheet mechanism) for low values of  $T$ . While the existing experimental evidence is not conclusive for the mechanisms operative at the micro-scale, the above hypothesis entails a dependence of the ductility on the Lode parameter, since shear dominated stress states are much more likely to promote the void sheet mechanism than axisymmetric states.

Classical models of ductile failure such as the Rice and Tracey (1969) void growth model and the Gurson (1977) yield criterion for an isotropic porous material were developed assuming spherical voids growing in a triaxial axisymmetric velocity field; and predict an exponential decrease in ductility with triaxiality consistent with the early experimental data on notched bars. However, they predict no dependence of damage growth on the Lode parameter, primarily due to the assumption of isotropy entailed by the self-similar growth of spherical voids and the focus on axisymmetric states. Widely used 'damage indicator' models, which specify evolution laws for a damage variable as a function of the loading path together with a failure criterion based on the attainment of a critical value of the damage variable, such as the Johnson and Cook (1985) model, are based on Rice and Tracey (1969)'s solution, and therefore insensitive to the Lode parameter. Recently, several authors have proposed alternative damage indicator models that include a Lode parameter dependence of the damage evolution law, by using phenomenological arguments and calibration with experimental data to determine the parameters in the model (Xue, 2007; Bai and Wierzbicki, 2008; Dunand and Mohr, 2011). These models retain the assumption of isotropy in the early micromechanical models and introduce the Lode parameter dependence by fiat. On the other hand, evidence from experimental micrographs (Barsoum and Faleskog, 2007; Pineau et al., 2016) and micromechanical cell model simulations (Nielsen et al., 2012) indicate that anisotropic effects due to void shape evolution are likely to play an important role in the failure process at low  $T$ .

Several anisotropic extensions of the Gurson model have been developed over the past decades (Gologanu et al., 1993; 1997; Kailasam and Castaneda, 1998; Benzerga and Besson, 2001; Monchiet et al., 2008; Keralavarma and Benzerga, 2008; 2010; Danas and Ponte Castañeda, 2009a; 2009b; Madou and Leblond, 2012a; 2012b), which attempt to capture the effect of material anisotropy due to void shape evolution and crystallographic texture on the constitutive response and damage rates. These models can, in principle, capture the apparent Lode parameter influence on the ductility, since the Lode parameter influences the evolution of the void shape and consequent anisotropy of the material. In fact, material anisotropy due to void shape evolution and non-radial loading path effects have been shown to lead to a similar Lode parameter dependence, and a non-monotonic dependence of the ductility on the triaxiality, as in the experiments (Benzerga et al., 2012; Danas and Ponte Castañeda, 2012; Thomas et al., 2016). However, the above models assume that plasticity is diffuse at the scale of the voids, and therefore preclude the possibility of shear strain localization in the inter-void ligaments as in the void sheet mechanism postulated earlier.

Periodic cell model simulations of porous representative volume elements (RVE) subjected to triaxial loadings have been used as an effective computational tool to study the micro-mechanisms of ductile failure (Tvergaard, 1981; Koplik and Needleman, 1988). Two-dimensional cell model analysis of void growth under axisymmetric proportional loading by Koplik and Needleman (1988) showed that the deformation in the RVE undergoes a transition from void growth by diffuse plastic flow at low porosities to void 'coalescence' by plastic collapse of the inter-void ligaments at high porosities. Under shear dominated stress states, analytical models show that yielding at the micro-scale of the voids is likely to occur preferentially by shear localization along a layer of voids in a periodic (Drucker, 1966; Leblond and Mottet, 2008) or random (Idiart and Ponte Castañeda, 2005; Keralavarma, 2017) array of voids. In order to study the loading path dependence of the microscopic deformation mechanisms, several groups have recently performed three-dimensional periodic cell model simulations of void growth under combined tension and shear (Barsoum and Faleskog, 2011; Dunand and Mohr, 2014; Tekoğlu et al., 2015; Luo and Gao, 2018). These studies reproduce the exponential decrease in ductility with increase in triaxiality  $T$  at a fixed value of the Lode parameter  $L$ , evidenced in the early two-dimensional studies. However, these studies also showed a characteristic non-monotonic dependence of the ductility on  $L$  at fixed  $T$ , with lower ductilities predicted for shear-dominated stress states ( $L$  near zero) compared to axisymmetric states ( $L = \pm 1$ ). Importantly, these studies showed that void coalescence, defined as the acceleration of void growth following a localization of plasticity in the inter-void ligaments, can occur due to a combination of tensile and shear strain localization in the inter-void ligaments.

One possibility to account for the transition in deformation mechanisms at the microscopic scale, within the framework of continuum damage-plasticity models, is to use a multi-surface approach; where the individual yield surfaces correspond to each possible mode of yielding within the RVE (see Pardo and Hutchinson, 2000; Benzerga, 2002; Tekoglu et al., 2012). Similar to the Gurson criterion for a porous material yielding by diffuse plastic flow, Thomason (1985) had proposed a semi-analytical criterion for void coalescence by internal necking between the voids under predominantly tensile loading of the ligament. A rigorous upper-bound analytical solution for the same problem was obtained recently by Benzerga and Leblond (2014). Torki et al. (2015) and Keralavarma and Chockalingam (2016) extended the above solution to account for localized yielding of the inter-void ligaments by a combination of the internal necking and shear localization modes. More recently, Keralavarma (2017) used the multi-surface approach to combine the Gurson yield criterion with the coalescence criterion of Keralavarma and Chockalingam (2016) to predict the effective yield locus for a statistically isotropic material containing a random distribution of equiaxed voids in a von Mises plastic matrix. All possible orientations of the potential coalescence bands at the scale of the voids were considered using a limit analysis approach, by assuming that the actual orientation of the coalescence band corresponds to the minimum yield stress for a given radial loading path in stress space. Comparison with numerically derived quasi-exact yield loci showed that the resulting criterion was in better agreement with the numerical data than the Gurson model; particularly for large values of the porosity and/or shear dominated loading paths (see Keralavarma, 2017).

The objective of the present paper is to perform a detailed comparison of the predictions of Keralavarma (2017)'s multi-surface model of void growth to coalescence (referred to simply as the multi-surface model in the following) with three dimensional cell model simulations under combined tension and shear similar to those reported by Barsoum and Faleskog (2011); Dunand and Mohr (2014). A periodic unit cell containing an initially spherical

concentric void, corresponding to a tetragonal lattice of voids in an isotropic von Mises matrix, will be monotonically loaded to failure under triaxial proportional loading conditions. Periodic boundary conditions will be imposed, and the “failure strain” of the RVE will be determined as the value of the macroscopic equivalent strain at which deformation localizes into a ligament connecting neighboring voids. The initial orientation of the unit cell relative to the principal directions of loading will be chosen to approximately minimize the effective ductility for a given loading path, so as to mimic the behavior of a random statistically isotropic aggregate of voids. The methodology for the unit cell simulations is explained in Section 2.1, followed by a summary of the simulation results in Section 2.2. The multi-surface plasticity model is summarized in Section 3, where a new phenomenological hardening law, applicable for both pre- and post-coalescence deformation of the RVE, is introduced in Section 3.2. Section 4 contains a detailed comparison of the model predictions for the loading path dependence of ductility with the cell model simulations, for nearly ideal plastic (Section 4.1) and strain hardening (Section 4.2) materials. Broader implications of the results are discussed in Section 5, followed by the conclusions of the study in Section 6.

**2. Periodic cell model simulations**

*2.1. Plasticity model, RVE and boundary conditions*

Consider a tetragonal lattice of spherical voids embedded in an elastic-plastic isotropic matrix, as shown in Fig. 1(a). The matrix is assumed to follow rate independent  $J_2$  flow theory with the Eulerian deformation rate tensor,  $\mathbf{d}$ , additively decomposed into elastic and plastic parts,  $\mathbf{d}^e$  and  $\mathbf{d}^p$ , respectively, as

$$\mathbf{d} = \mathbf{d}^e + \mathbf{d}^p \tag{1}$$

The elastic strain rate is related to the Cauchy stress,  $\boldsymbol{\sigma}$ , via a hypoelastic constitutive law

$$\overset{\nabla}{\boldsymbol{\sigma}} = \mathbb{C} : \mathbf{d}^e \tag{2}$$

where  $\mathbb{C}$  is the fourth order elastic stiffness tensor and  $\overset{\nabla}{\boldsymbol{\sigma}}$  denotes the Jaumann rate of  $\boldsymbol{\sigma}$ . The plastic deformation rate  $\mathbf{d}^p$  derives from the yield function via the normality property

$$\mathbf{d}^p = \dot{\lambda} \frac{\partial \mathcal{F}}{\partial \boldsymbol{\sigma}}, \quad \mathcal{F}(\boldsymbol{\sigma}) := \sigma_{eq} - \bar{\sigma} \tag{3}$$

where  $\mathcal{F}(\boldsymbol{\sigma}) \leq 0$  is the von Mises yield function,  $\dot{\lambda} \geq 0$  is the plastic multiplier,  $\sigma_{eq} := \sqrt{\frac{3}{2} \boldsymbol{\sigma}' : \boldsymbol{\sigma}'}$  is the Mises equivalent stress,  $\boldsymbol{\sigma}'$  is the stress deviator and  $\bar{\sigma}$  is the instantaneous flow stress of the material. The latter is given by a power law hardening equation of

the form

$$\bar{\sigma} = \sigma_0 \left( 1 + \frac{\varepsilon_{eq}^p}{\varepsilon_0} \right)^n \tag{4}$$

where  $\sigma_0$  is the initial yield stress,  $\varepsilon_0$  is a constant reference strain,  $n$  is the hardening exponent and  $\varepsilon_{eq}^p$  is the equivalent plastic strain, which evolves with the plastic strain rate  $\mathbf{d}^p$  according to the relation

$$\dot{\varepsilon}_{eq}^p = \sqrt{\frac{2}{3} \mathbf{d}^p : \mathbf{d}^p} \tag{5}$$

In the rate independent limit, the plastic multiplier  $\dot{\lambda}$  is determined using the consistency condition  $\dot{\lambda} \dot{\mathcal{F}} = 0$ .

The effective macroscopic constitutive behavior of the porous material is investigated by loading the tetragonal RVE shown in Fig. 1(b) along a radial loading path in stress space, subjected to periodic boundary conditions. The dimensions of the RVE correspond to the inter-void spacing in Fig. 1(a), which is assumed to be smallest in the transverse plane; i.e.  $c \geq a$ . The macroscopic stress,  $\boldsymbol{\Sigma}$ , and deformation rate,  $\mathbf{D}$ , tensors are obtained through volume averaging of the corresponding microscopic quantities within the framework of Hill–Mandel homogenization theory; i.e.

$$\boldsymbol{\Sigma} = \langle \boldsymbol{\sigma} \rangle_V, \quad \mathbf{D} = \langle \mathbf{d} \rangle_V \tag{6}$$

where the notation  $\langle \cdot \rangle_V$  denotes averaging over  $V$ , the volume of the RVE in the current configuration. Analogous to Eq. (1), the macroscopic deformation rate can be decomposed into elastic and plastic parts,  $\mathbf{D} = \mathbf{D}^e + \mathbf{D}^p$ , where the macroscopic elastic and plastic deformation rates,  $\mathbf{D}^e$  and  $\mathbf{D}^p$  respectively, are volume averages of the corresponding microscopic quantities. Under radial loading, the ratios of the components of  $\boldsymbol{\Sigma}$  remain constant throughout the loading history, and can be written as a function of the two loading path parameters introduced earlier, the stress triaxiality  $T$  and the Lode parameter  $L$ , and the orientation of the RVE relative to the principal directions of loading.  $T$  and  $L$  are related to the invariants of  $\boldsymbol{\Sigma}$  as

$$T = \frac{\Sigma_m}{\Sigma_{eq}}, \quad L = -\frac{27 \det(\boldsymbol{\Sigma}')}{2 \Sigma_{eq}^3} \tag{7}$$

where  $\Sigma_m = \frac{1}{3} \text{tr}(\boldsymbol{\Sigma})$  is the mean stress,  $\Sigma_{eq} = \sqrt{\frac{3}{2} \boldsymbol{\Sigma}' : \boldsymbol{\Sigma}'}$  is the macroscopic equivalent stress and  $\boldsymbol{\Sigma}'$  is the deviator of  $\boldsymbol{\Sigma}$ . The orientation of the RVE relative to the principal directions of loading is chosen such as to approximately minimize the ductility as explained below.

The effective mechanical behavior of the RVE shown in Fig. 1(b) is expected to be orthotropic in the Cartesian basis shown in the figure; with equal yield stresses in the  $\mathbf{e}_1$  and  $\mathbf{e}_3$  directions due to the tetragonal symmetry. In the special case of equal void spacing in the axial and transverse directions, i.e.  $c = a$ , the effective response will have cubic symmetry. However, if the initial porosity of the material is low ( $\leq 0.001$ ), as is the case in all the simulations reported here, the equivalent elasto-plastic response of the RVE at small strains is known from prior cell model studies to be approximately isotropic; dependent only on the void volume fraction and independent of the aspect ratio of the unit cell (Koplik and Needleman, 1988). On the other hand, at large plastic strain and porosity levels, neighboring voids begin to interact through the plastic strain fields in the inter-void ligaments, following which void coalescence occurs by plastic strain localization along a band of voids. The condition for the onset of coalescence depends on the thickness of the inter-void ligaments in the direction of coalescence; i.e. the strain to the onset of coalescence will be clearly different for a cubic and tetragonal lattice of voids at the same porosity. The onset of coalescence is usually followed by

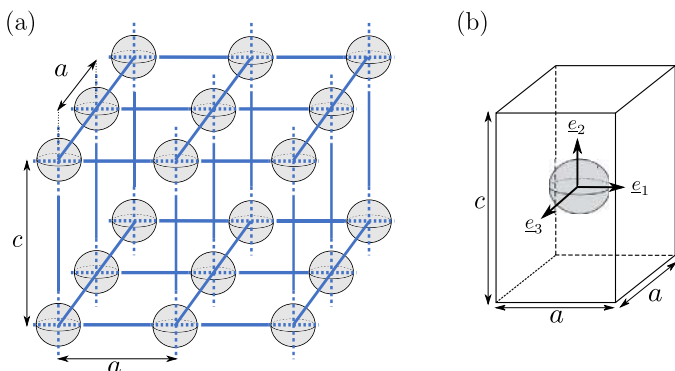


**Fig. 1.** (a) Periodic tetragonal lattice of spherical voids. (b) Representative volume element containing a single concentric void.

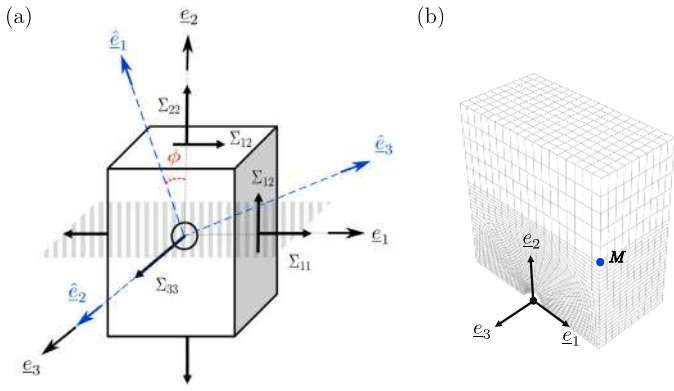


**Fig. 2.** (a) Orientation of the RVE relative to the principal directions of stress. (b) Structured mesh used in the finite element computations for a quadrant of the RVE. The location of the point  $M$ , used to compute the localization indicator, is also shown.

accelerated growth of porosity inside the band, associated with a rapid drop in the overall flow stress, and eventual material separation. Since the latter is not accounted for in the simulations, the ductility of the material for a given loading path will be quantified by the equivalent strain to the onset of void coalescence, when plasticity first localizes into a band connecting neighboring voids.

Continuum studies of plastic strain localization in a general class of dilatant elasto-plastic materials by Rudnicki and Rice (1975) had shown that localization tends to occur first along a band with its normal perpendicular to the intermediate principal stress direction. Further, analysis of the onset of coalescence in a random distribution of equiaxed voids by Keralavarma (2017) showed that the normal to the plane of coalescence must be orthogonal to a principal direction, which is usually found to be the intermediate stress direction at low to moderate porosities relevant to ductile fracture studies. Motivated by the above results, we orient the  $c$ -axis of the tetragonal RVE perpendicular to the intermediate principal stress direction, as illustrated in Fig. 2(a). The triad associated with the principal axes of the RVE is denoted  $\underline{e}_1, \underline{e}_2, \underline{e}_3$  in Fig. 2(a), and the principal directions of stress are denoted  $\hat{\underline{e}}_1, \hat{\underline{e}}_2, \hat{\underline{e}}_3$ , corresponding to the principal stresses  $\Sigma_1 \geq \Sigma_2 \geq \Sigma_3$  respectively. The  $\underline{e}_3$  axis of the RVE is taken to coincide with the intermediate principal direction  $\hat{\underline{e}}_2$ , while the  $c$ -axis of the RVE (collinear with base vector  $\underline{e}_2$ ) makes an angle  $\phi$  with the major principal stress direction  $\hat{\underline{e}}_1$ . The value of  $\phi$  is chosen such that the expected orientation of the localization band coincides approximately with the material plane with the highest packing density of voids (or smallest inter-void ligament thicknesses), which is the transverse plane for the tetragonal RVE, shown shaded in Fig. 2(a). By this device of choosing the loading orientation to approximately minimize the strain to coalescence for a given loading path in stress space, we seek to approximate the behavior of a random statistically isotropic aggregate of voids in our cell model simulations.

Given the choice of the RVE orientation in Fig. 2(a), the components of the average shear stress on the  $\underline{e}_3$  faces of the RVE (i.e. the faces with normal  $\pm \underline{e}_3$ ) vanish, and the non-zero components of the macroscopic stress tensor acting on the faces of the RVE are marked in Fig. 2(a). The resulting deformation involves warping of the  $\underline{e}_1$  and  $\underline{e}_2$  faces of the RVE, while the  $\underline{e}_3$  faces remain planar. Exploiting this fact, together with the point symmetry of the deformation in the  $\underline{e}_1 - \underline{e}_2$  plane about the center of the void, only a quadrant of the unit cell shown in Fig. 2(b) is meshed and analyzed using the commercial finite element software, Abaqus/Standard, version 6.10. The boundaries of the domain perpendicular to  $\underline{e}_3$  are constrained to remain planar while periodicity conditions are

imposed on the remaining boundaries. A structured mesh consisting of fully integrated 8-node linear brick elements is used. A refined grid is used along the void boundary and the transverse inter-void ligament regions in order to capture the strain localization accurately; while a coarser grid is used away from the voids in the axial direction of the cell, as shown in Fig. 2(b).

The loading is imposed by prescribing the average normal displacements of the nodes on the boundary together with a simple shear deformation in the  $\underline{e}_1 - \underline{e}_2$  plane. Let  $\pm U_i$  denote the average normal displacements of the nodes on a periodic boundary (i.e. a boundary that does not intersect the void) with unit normal  $\pm \underline{e}_i$  ( $i = 1..3$ ). In addition, simple shear in the  $\underline{e}_1 - \underline{e}_2$  plane is imposed by prescribing the average tangential displacement,  $U_T$ , of the nodes on the top boundary, with normal  $\underline{e}_2$ , in the  $\underline{e}_1$  direction. Periodicity of the deformation, and the symmetry conditions on the boundaries that intersect the void, are enforced using multi-point constraint equations given in Appendix A (also see Tekoglu, 2014; Dunand and Mohr, 2014). The boundary conditions are designed such that the anti-symmetric warping of the boundaries of the RVE on the  $\underline{e}_1 - \underline{e}_2$  section planes due to shear is captured, while the  $\underline{e}_3$  faces are constrained to remain planar due to symmetry.

The components of the average deformation gradient,  $\mathbf{F}$ , due to the imposed average boundary displacements  $U_i$ , in the principal frame of the cell, can be written as

$$[\mathbf{F}] = \begin{bmatrix} 1 + \frac{2U_1}{D_1} & \frac{2U_T}{D_2} & 0 \\ 0 & 1 + \frac{2U_2}{D_2} & 0 \\ 0 & 0 & 1 + \frac{2U_3}{D_3} \end{bmatrix} \quad (8)$$

where  $D_i$  ( $i = 1..3$ ) denotes the length of the RVE in the  $\underline{e}_i$  direction in the reference configuration. For the tetragonal RVE shown in Fig. 2(a),  $D_1 = D_3 = a$  and  $D_2 = c$ . The macroscopic deformation rate tensor,  $\mathbf{D}$ , work conjugate to  $\Sigma$  is obtained as the symmetric part of the macroscopic velocity gradient tensor,  $\mathbf{L} = \dot{\mathbf{F}}\mathbf{F}^{-1}$ . The components of  $\mathbf{D}$  in the above Cartesian frame read

$$[\mathbf{D}] = \begin{bmatrix} \frac{2\dot{U}_1}{d_1} & \frac{\dot{U}_T}{d_2} - \frac{2U_T\dot{U}_1}{d_1d_2} & 0 \\ \frac{\dot{U}_T}{d_2} - \frac{2U_T\dot{U}_1}{d_1d_2} & \frac{2\dot{U}_2}{d_2} & 0 \\ 0 & 0 & \frac{2\dot{U}_3}{d_3} \end{bmatrix} \quad (9)$$

where  $d_i = D_i + 2U_i$  are the average lengths of the RVE along the respective coordinate directions in the current configuration.

Radial loading implies that the components of  $\Sigma$  vary in proportion; such that the normalized stress tensor,  $\mathbf{S} := \Sigma / \Sigma_{\text{eq}}$ , remains constant and can be written as a function of the loading path parameters  $T$  and  $L$ , and the orientation of the RVE given by the angle  $\phi$  between the major principal stress direction  $\hat{\underline{e}}_1$  and the  $c$ -axis of the RVE; see Fig. 2(a). Expressions for the components of the normalized stress tensor  $\mathbf{S}(T, L, \phi)$  are given in Appendix B. The rate of work done per unit volume of the RVE in the current configuration can therefore be written as

$$\Sigma : \mathbf{D} = \Sigma_{\text{eq}} \dot{E}_{\text{eq}} \quad (10)$$

where  $\dot{E}_{\text{eq}} := \mathbf{S} : \mathbf{D}$  is a macroscopic equivalent strain rate work conjugate to  $\Sigma_{\text{eq}}$ . Using Eq. (9) and the definition of the normalized stress tensor  $\mathbf{S}$  in (10),  $\dot{E}_{\text{eq}}$  can be written as

$$\dot{E}_{\text{eq}} = \left( \frac{2S_{11}}{d_1} - \frac{4S_{12}U_T}{d_1d_2} \right) \dot{U}_1 + \left( \frac{2S_{22}}{d_2} \right) \dot{U}_2 + \left( \frac{2S_{33}}{d_3} \right) \dot{U}_3 + \left( \frac{2S_{12}}{d_2} \right) \dot{U}_T \quad (11)$$

The loading is imposed on the RVE through a set of four additional nodes, exterior to the mesh shown in Fig. 2(b), whose instantaneous velocities are equated with the average displacement rates of the RVE boundaries,  $\dot{U}_1, \dot{U}_2, \dot{U}_3$  and  $\dot{U}_T$ , through equation constraints. The total rate of work done on RVE therefore equals

$$\Sigma_{\text{eq}} \dot{E}_{\text{eq}} V = F_1 \dot{U}_1 + F_2 \dot{U}_2 + F_3 \dot{U}_3 + F_T \dot{U}_T \quad (12)$$

where  $F_1, F_2, F_3, F_T$  are the forces acting on the respective nodes in their direction of motion. Using (11) in (12), it follows that the forces  $F_i$  ( $i = 1, 2, 3, T$ ) must be in proportion to the corresponding coefficients of  $\dot{U}_i$  in (11); i.e.

$$F_1 : F_2 : F_3 : F_T = \left( \frac{2S_{11}}{d_1} - \frac{4S_{12}U_T}{d_1 d_2} \right) : \left( \frac{2S_{22}}{d_2} \right) : \left( \frac{2S_{33}}{d_3} \right) : \left( \frac{2S_{12}}{d_2} \right) \quad (13)$$

Radial loading of the RVE is ensured by imposing the above proportionality constraint between the nodal forces. This is done by using a linear multi-point constraint equation relating prescribed velocity,  $\dot{U}_0$ , of a fifth master node and the velocities of the above four slave nodes, as

$$\left( \frac{2S_{11}}{d_1} - \frac{4S_{12}U_T}{d_1 d_2} \right) \dot{U}_1 + \left( \frac{2S_{22}}{d_2} \right) \dot{U}_2 + \left( \frac{2S_{33}}{d_3} \right) \dot{U}_3 + \left( \frac{2S_{12}}{d_2} \right) \dot{U}_T = \dot{U}_0 \quad (14)$$

where the coefficients of  $\dot{U}_1, \dot{U}_2, \dot{U}_3$  and  $\dot{U}_T$  are proportional to the respective nodal forces according to (13); see Zhu et al. (2018) for details. Recall that  $d_i = D_i + 2U_i$  are the average cell dimensions in the current configuration, so that for constant  $\mathbf{S}$ , the ratios of  $F_i$  evolve as a function of time.

## 2.2. Simulation results

The effective response of the RVE shown in Fig. 2 subjected to proportional stressing (constant  $T$  and  $L$ ) is examined by plotting the macroscopic equivalent stress  $\Sigma_{\text{eq}}$  and the porosity  $f$  as a function of the macroscopic equivalent strain,  $E_{\text{eq}}$ , obtained as

$$E_{\text{eq}} = \int_0^t \dot{E}_{\text{eq}} dt \quad (15)$$

with  $\dot{E}_{\text{eq}}$  given by (11). The matrix is assumed to be isotropic, and follow rate independent  $J_2$  elasto-plastic model with power-law hardening, as discussed in Section 2.1. Material properties are Young's modulus  $E = 210$  GPa, Poisson's ratio  $\nu = 0.3$ , initial yield stress  $\sigma_0 = 420$  MPa, hardening exponent  $n = 0.1$  and the reference strain  $\varepsilon_0 = 0.002$  in Eq. (4). The void is assumed to be initially spherical with a volume fraction  $f_0 = 0.001$ . The orientation of the RVE relative to the major principal stress direction, i.e. the angle  $\phi$  in Fig. 2, is chosen such that the effective ductility is minimized for a given  $T$  and  $L$ . This minimization is performed by trial and error by varying the value of  $\phi$  in discrete intervals over the range  $0^\circ$ – $45^\circ$ . It is observed that, irrespective of the loading path, the minimum ductility occurs for some value of  $\phi$  in the range  $36^\circ$ – $45^\circ$ , in agreement with earlier results reported by Barsoum and Faleskog (2011) using similar unit cells. Moreover, predictions for the orientation of the coalescence plane using the multi-surface model, described in Section 3, falls in the range  $40^\circ < \phi \leq 45^\circ$  over a wide range of values of  $T$  and  $L$ . It is also observed that the variation of the predicted ductility within the above range of  $\phi$  is small in comparison to the variation of ductility as a function of  $T$  and  $L$ , so that, unless mentioned otherwise, all the simulation results are shown for a constant value of  $\phi = 45^\circ$ . The effect of varying  $\phi$  on the ductility will be shown in Fig. 6, which illustrates the accuracy of this approximation.

Fig. 3(a) shows a comparison of the equivalent stress-strain response obtained in the simulations performed for two values of the cell aspect ratio,  $\alpha := c/a$ , corresponding to cubic ( $\alpha = 1$ ) and tetragonal ( $\alpha = 2$ ) symmetry. Corresponding results for the evolution of the porosity  $f$  as a function of  $E_{\text{eq}}$  are shown in Fig. 3(b). Results are shown for three different values of the stress triaxiality  $T = 2/3, 1$  and  $2$ , and a constant value of the Lode parameter  $L = -1$ , corresponding to axisymmetric stress states with major axial stress,  $\Sigma_1 > \Sigma_2 = \Sigma_3$ . The results in Fig. 3(a) and (b) show that, for all values of  $T$  shown, the unit cell response during the initial hardening stage is independent of the aspect ratio of the cell. This is consistent with the findings from earlier cell model studies (Koplik and Needleman, 1988) that void growth for dilute values of the porosity is independent of the distribution of the voids. However, at large values of the equivalent strain, neighboring voids begin to interact through the plastic strain fields in the inter-void ligaments, resulting in rapid softening and accelerated damage growth by strain localization in the ligaments, referred to as void coalescence.

The onset of coalescence, which is a precursor to ductile fracture, is characterized by the instance when plastic deformation starts to intensify in a narrow band, while the material outside the band undergoes elastic unloading. The width,  $W$ , of the localization band is known to be of the order of the void diameter, except for highly oblate penny shaped voids (Benzerga, 2002; Morin et al., 2015). In order to detect the onset of coalescence, the quarter cell in Fig. 2(b) is divided into lower and upper blocks corresponding to  $0 < X_2 < B/2$  and  $B/2 < X_2 < D_2/2$  respectively ( $W \ll B < D_2$ ), such that when plastic deformation localizes into a band of width  $W$  containing the void, the upper block,  $X_2 > B/2$ , undergoes elastic unloading. The average deformation gradient of the upper block,  $\mathbf{F}_u$ , is calculated as follows using the displacement,  $\underline{u}^M$ , of a reference point  $M$  at  $(D_1/2, B/2, 0)$ ; see Fig. 2(b).

$$[\mathbf{F}_u] = \begin{bmatrix} 1 + \frac{2U_1}{D_1} & \frac{2(U_T - u_1^M + U_1)}{(D_2 - B)} & 0 \\ 0 & 1 + \frac{2(U_2 - u_2^M)}{(D_2 - B)} & 0 \\ 0 & 0 & 1 + \frac{2U_3}{D_3} \end{bmatrix} \quad (16)$$

Following Dunand and Mohr (2014); Needleman and Tvergaard (1992), a scalar localization indicator,  $\xi$ , is defined as

$$\xi = \frac{\|\dot{\mathbf{F}}\|}{\|\dot{\mathbf{F}}_u\|} \quad (17)$$

where  $\mathbf{F}$  and  $\mathbf{F}_u$  are the deformation gradients of the RVE and the upper block respectively, and  $\|\cdot\|$  denotes the Euclidean norm of a tensor. Assuming  $B \gg W$  and the elastic strains are negligibly small compared to the plastic strains, the onset of localization corresponds to  $\xi \rightarrow \infty$ . In practice, small finite increments of  $\mathbf{F}$  are used in place of the rates in Eq. (17) to compute  $\xi$  and localization is assumed to have occurred when the value of  $\xi$  exceeds an arbitrarily defined cutoff value of 10. The value of  $B$  is chosen as  $B = a$  for the tetragonal RVE and  $B = 0.8a$  for the cubic RVE in the results shown in Fig. 3.

The variation of  $\xi$  as a function of  $E_{\text{eq}}$  for the simulations in Fig. 3(a) and (b) is shown in Fig. 3(c); and the onset of coalescence, as determined using the above criterion, is indicated by the  $\times$  symbol in all the figures. The value of the localization indicator  $\xi$  remains close to unity during initial void growth by diffuse plastic flow. The onset of coalescence corresponds to a sharp increase in the value of  $\xi$  over a short interval of strain, following which the curve becomes almost vertical. While the  $\times$  marks in Fig. 3(c) corresponds to  $\xi = 10$ , it is clear that the strain to coalescence is insensitive to this choice; provided the value of the cutoff is

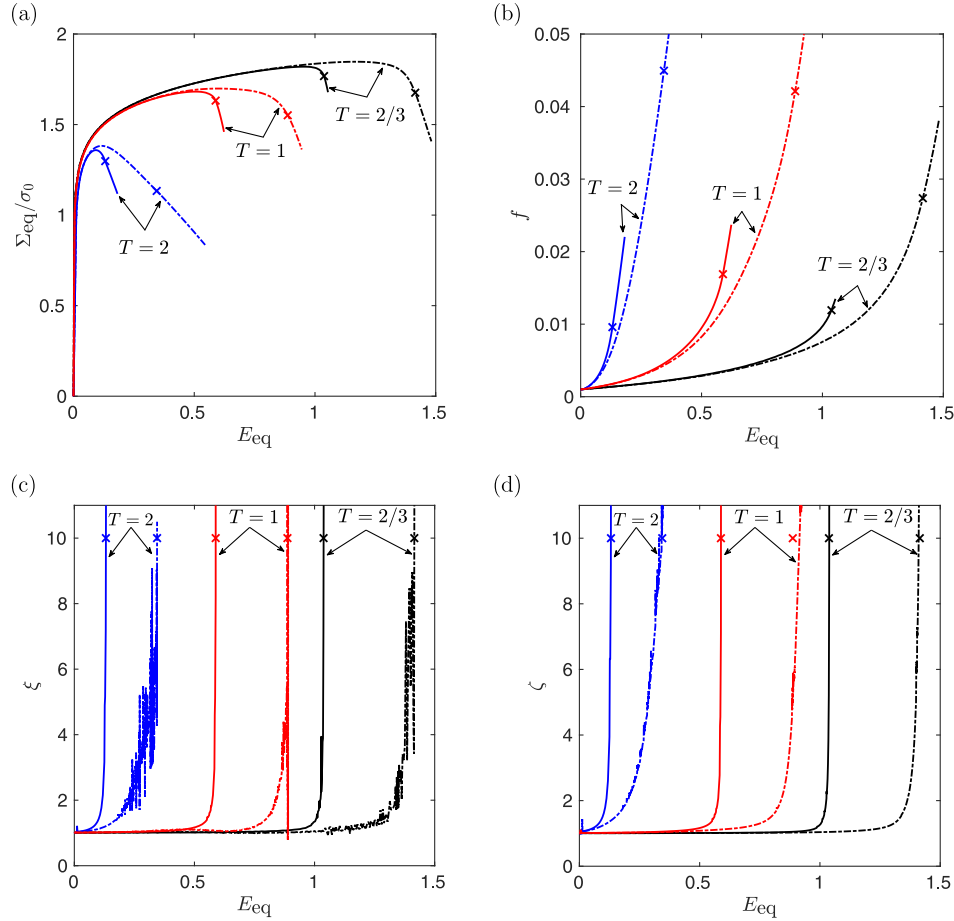


**Fig. 3.** Effective response of a tetragonal RVE with aspect ratio  $\alpha = 2$  (solid lines) and a cubic RVE with aspect ratio  $\alpha = 1$  (dashed lines) subjected to proportional stressing with  $L = -1$  and varying  $T$ : (a) normalized equivalent stress  $\Sigma_{eq}/\sigma_0$  vs. equivalent strain  $E_{eq}$ , (b) porosity  $f$  vs  $E_{eq}$ , (c) localization indicator  $\xi$  vs  $E_{eq}$ , and (d) localization indicator  $\zeta$  vs  $E_{eq}$ . The  $\times$  marks in all the figures correspond to the onset of coalescence according to the criterion  $\xi = 10$ .

sufficiently large. The equivalent strain to the onset of coalescence,  $E_{eq}^c$ , will be used in the remainder of this paper as a measure of the intrinsic ductility of the material under proportional loading paths. It can be seen from Fig. 3(a) and (b) that the value of  $E_{eq}^c$  decreases as a function of  $T$  for both RVE shapes considered. The effect of triaxiality on the ductility observed in Fig. 3 has been well characterized from several cell model studies in the literature as well as theoretical models. Fig. 3 also shows that, at fixed  $T$ , the strain to the onset of coalescence is significantly lower for the tetragonal cell (solid lines) compared to the cubic cell (dashed lines). Void coalescence occurs due to plastic collapse of the intervoid ligaments, the condition for which clearly depends on the ligament thickness. Hence, the tetragonal RVE with a smaller initial ligament thickness in the transverse direction shows lower strains to coalescence than the cubic RVE.

Comparison of the localization indicators in Fig. 3(c) also shows that the value of  $\xi$  shows rapid high amplitude oscillations during the transition to coalescence in the case of the cubic RVE, which is absent in the case of the tetragonal RVE. Upon further examination, it turns out that this is due to the value of  $B = 0.8a$  not being sufficiently large compared to the width of the localization band for the cubic RVE; so that part of the localized strain field extends up to the point  $M$  used to compute  $\mathbf{F}_u$  in (16). An alternate localization indicator,  $\zeta$ , can be defined by looking at the ratio of the average plastic dissipation rate in the RVE,  $\dot{\Pi}$ , to the average plastic dissipation rate in the upper block,  $\dot{\Pi}_u$ , as

$$\zeta = \frac{\dot{\Pi}}{\dot{\Pi}_u} \quad (18)$$

Fig. 3(d) shows the variation of  $\zeta$  as a function of  $E_{eq}$ , superposed with  $\times$  marks corresponding to the values of  $E_{eq}^c$  determined using the other localization indicator  $\xi$ . It is clear that both localization indicators show similar variation with  $E_{eq}$  as well as predicts identical value of  $E_{eq}^c$  in the case of the tetragonal RVE. For the cubic RVE, the variation of  $\zeta$  with  $E_{eq}$  is somewhat different and shows much lower noise compared to  $\xi$ . Further, the value of the failure strains predicted by the two localization indicators are slightly different in some cases, such as  $T = 1$ . In fact, simulations performed for some values of  $L$  (e.g.  $L \approx 1$ ) shows that neither of the localization criteria discussed above is satisfied up to very large values of  $E_{eq}$ , in the case of the cubic RVE. This indicates that the cubic distribution of voids has difficulty in achieving localization in the transverse direction for certain loading paths. A possible reason for this is the phenomenon of necklace coalescence (coalescence between voids along the major stress direction), which has been observed in the case of a cubic distribution of voids in some recent cell model studies (Luo and Gao, 2018); although precluded by the boundary conditions in the present case. On the other hand, a clear transition to coalescence in the transverse direction is obtained over a much wider range of values of  $T$  and  $L$  for the tetragonal RVE; so that the results in the remainder of the paper will be shown for the tetragonal RVE with aspect ratio  $\alpha = 2$ .

The effective response of the tetragonal RVE as a function of the Lode parameter  $L$  for fixed  $T = 1$  is shown in Fig. 4. The range of variation of  $L$  is  $[-1, 1]$  with a value of  $-1$  for axisymmetric stress states with major axial stress,  $+1$  for axisymmetric stress states with major lateral stress and zero for generalized shear loadings (pure shear with superposed hydrostatic stress). Intermediate

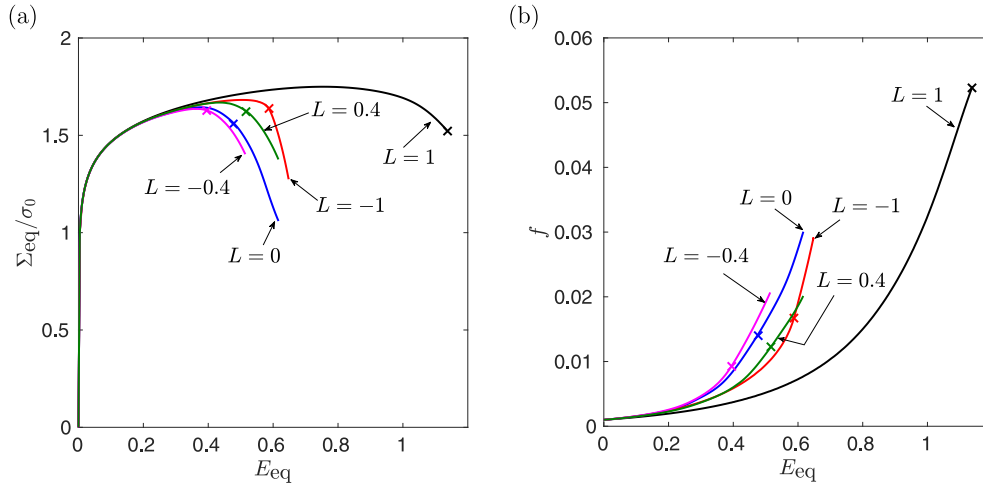


**Fig. 4.** Effective response of a tetragonal RVE with aspect ratio  $\alpha = 2$  subjected to proportional stressing with  $T = 1$  and varying  $L$ : (a) normalized equivalent stress  $\Sigma_{eq}$  vs. equivalent strain  $E_{eq}$ , (b) porosity  $f$  vs  $E_{eq}$ . The  $\times$  marks indicate the onset of coalescence according to the criterion  $\xi = 10$ .

values of  $L$  correspond to a combination of axisymmetric and shear loadings. The effective stress-strain response for five different values of  $L$  are shown in Fig. 4(a), and the corresponding porosity curves are shown in Fig. 4(b). The onset of coalescence, indicated by the  $\times$  marks, is determined using the condition  $\xi = 10$  in this and all subsequent figures; since both the localization indicators discussed above predict identical results for the tetragonal RVE. It is clear that axisymmetric loading paths with  $L = \pm 1$  yield higher ductilities compared to shear dominated loadings. The lowest ductility is predicted for  $L = -0.4$ . The effect of the sign of  $L$  (equivalently the sign of the determinant of the deviatoric stress  $J_3$ ; see Eq. (7)) is also visible, with positive values of  $L$  yielding higher ductilities compared to negative values. Similar trends are observed also in the porosity curves of Fig. 4(b), with axisymmetric states showing slower void growth compared to shear dominated loading paths. Although the above results are shown for a specific value of  $T = 1$ , qualitatively similar results are obtained over a wide range of (positive) values of  $T$ . The results obtained are consistent with

other recent cell model studies of void growth under combined tension and shear (Barsoum and Faleskog, 2011; Dunand and Mohr, 2014; Tekoğlu et al., 2015; Luo and Gao, 2018), all of which predict reduced ductility under shear dominated loading paths compared to axisymmetric loading at fixed triaxiality.

Fig. 5 shows the contours of microscopic equivalent plastic strain  $\epsilon_{eq}^p$  plotted on the deformed configuration of the cell, at a relatively large value of the effective strain  $E_{eq}$  just prior to the onset of coalescence. For ease of comparison of the void shapes, only a rectangular sub-domain centered on the void is shown. Fig. 5(a) shows the contours for  $T = 2$  at  $E_{eq} = 0.1$  and three different values of  $L = -1, 0$  and  $+1$ , while Fig. 5(b) shows similar contours for  $T = 2/3$  at  $E_{eq} = 0.7$ . The void retains a more or less equiaxed shape up to the onset of coalescence for  $T = 2$ , due to the relatively high hydrostatic stress levels. Further, the effect of  $L$  on void growth is also visible with the average void size being largest for  $L = 0$  and smallest for  $L = 1$  at constant effective strain. For  $T = 2/3$ , the void shape evolves significantly from an initial sphere

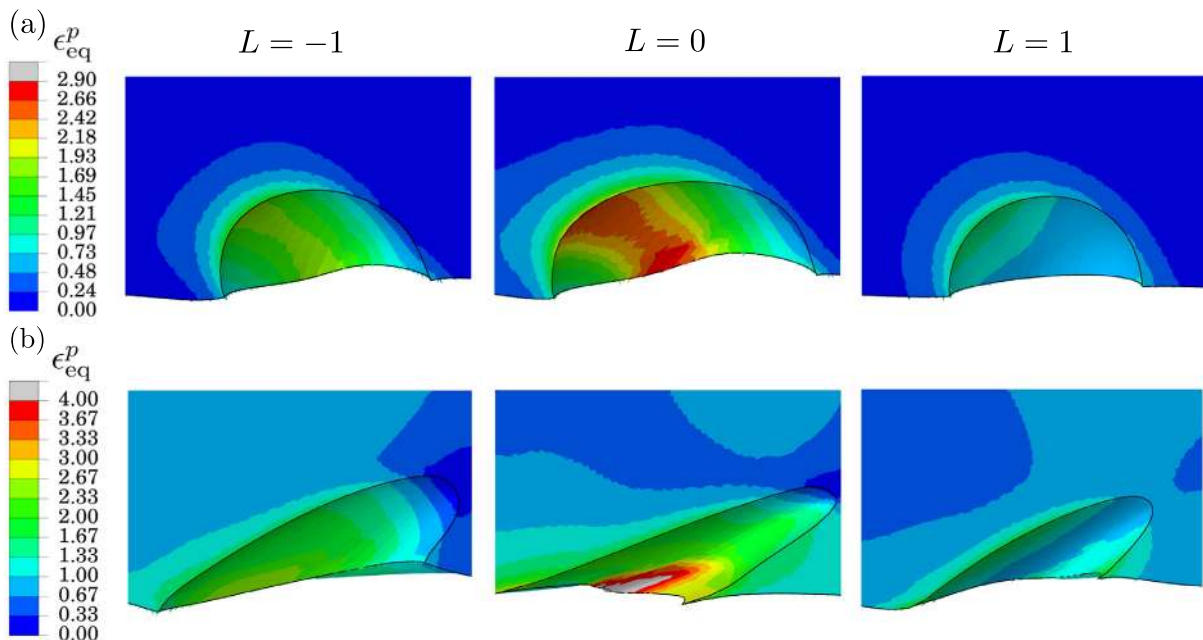


**Fig. 5.** Contours of microscopic equivalent plastic strain  $\epsilon_{eq}^p$  on the deformed configuration of the unit cell at a constant value of  $E_{eq}$ , constant  $T$  and varying  $L$ : (a)  $E_{eq} = 0.1$  and  $T = 2$ , (b)  $E_{eq} = 0.7$  and  $T = 2/3$ . Only a small rectangular sub-domain centered on the void is shown.

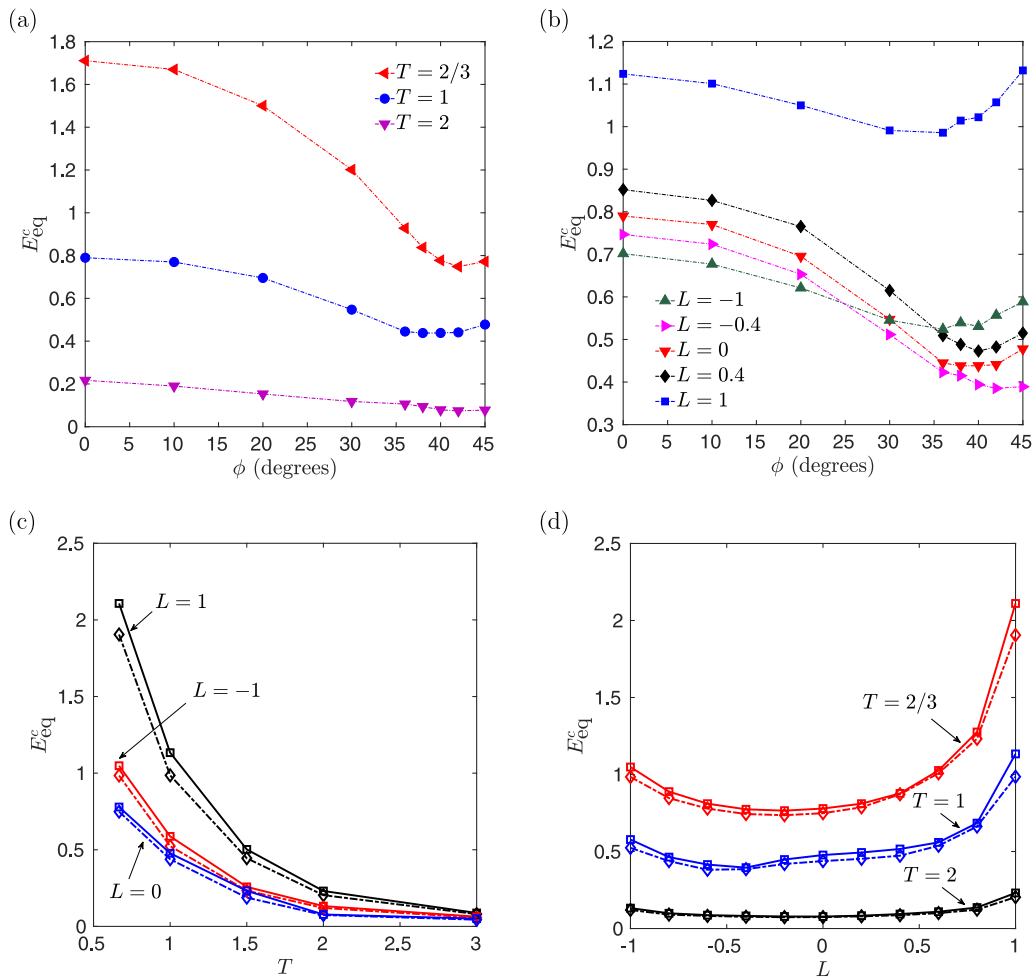


**Fig. 6.** Effect of loading orientation on the macroscopic equivalent strains to coalescence  $E_{eq}^c$  for (a)  $L = 0$  and several values of  $T$ , and (b)  $T = 1$  and several values of  $L$ . The failure loci,  $E_{eq}^c$  as a function of (c)  $T$  for several values of  $L$  and (d)  $L$  for several values of  $T$ . The solid lines in (c)–(d) corresponds to a fixed RVE orientation given by  $\phi = 45^\circ$  in Fig. 2(a), while the dashed lines correspond to the minimum ductility over all loading orientations considered in (a) and (b).

to a highly non-equiaxed ellipsoid, and the principal axes of the void also rotate as a result of the imposed shear deformation in the transverse plane of the RVE. Hence, the induced anisotropy in the effective response of the RVE will be significantly higher for lower values of  $T$ . Unlike in Fig. 5(a), the effect of  $L$  on void growth is not obvious from Fig. 5(b) due to the significant distortion of the void shape, which is largest in the case of generalized shear ( $L = 0$ ).

Simulations of the type shown in Figs. 3 and 4 have been performed over a wide range of values of  $T$  and  $L$ , and several loading orientations defined by the orientation angle  $\phi$  between the  $c$ -axis of the RVE and the major loading axis  $\hat{e}_1$  in Fig. 2(a). Fig. 6 shows a summary of the ductility predictions obtained using the localization criterion discussed above. For a fixed value of  $L = 0$ , Fig. 6(a) shows the variation of the equivalent strains to the onset of coalescence  $E_{eq}^c$  as a function of the RVE orientation angle  $\phi$  for several values of  $T$ . Similarly, Fig. 6(b) shows the variation of  $E_{eq}^c$  with  $\phi$  for  $T = 1$  and several values of  $L$ . It is clear from these plots that, irrespective of the values of  $T$  and  $L$ , minimum ductility is predicted for  $36^\circ \leq \phi \leq 45^\circ$ ; in agreement with the results of Barsoum and Faleskog (2011). Fig. 6(c) shows the variation of  $E_{eq}^c$  as a function of  $T$  for constant values of  $L = -1, 0$  and  $1$ ; while Fig. 6(d) shows the variation of  $E_{eq}^c$  as a function of  $L$  for constant values of  $T = 2/3, 1$  and  $2$ . The points connected by dashed lines in Figs. 6(c) and (d) correspond to the minimum value of  $E_{eq}^c$  obtained over all loading orientations considered in Fig. 6(a) and (b). The points con-

nected by solid lines of the same color correspond to the value of  $E_{eq}^c$  obtained in the simulations for a fixed value of  $\phi = 45^\circ$ . The results in Figs. 6(c) and (d) show that the difference between the values of  $E_{eq}^c$  for the minimum ductility orientation and  $\phi = 45^\circ$  is small compared to the effect of the loading parameters  $T$  and  $L$  on the ductility. Therefore, all the simulations in Section 4 and the comparison with the analytical model will be done assuming  $\phi = 45^\circ$ .

The effect of the triaxiality on  $E_{eq}^c$  shown in Fig. 6(c) is consistent with an exponential decrease in ductility observed in several earlier cell model studies. However, the figure also clearly illustrates the Lode parameter dependence of ductility, since the curves for the different values of  $L$  diverge for values of  $T < \sim 3$ . Highest ductility is predicted for axisymmetric loadings with major lateral stress ( $L = 1$ ), while lowest ductility is predicted for generalized shear loadings ( $L = 0$ ). Similar trends as in Fig. 6(c) have also been reported by Tekoğlu et al. (2015) (see Fig. 14 of that paper). The effect of the Lode parameter on ductility at fixed triaxiality is illustrated in Fig. 6(d) for three different values of  $T$ . The curves of  $E_{eq}^c$  vs.  $L$  have approximately convex shapes with the minimum ductility predicted for some negative value of  $L$ , consistent with the trends reported in the recent studies by Barsoum and Faleskog (2011); Dunand and Mohr (2014) and others. In the Section 4, we compare the predicted stress-strain response and strains to the onset of coalescence from the cell model simulations with corresponding predictions from the recently developed

multi-surface porous plasticity model of Keralavarma (2017), summarized in the following section.

### 3. Multi-surface porous plasticity model

#### 3.1. Yield criterion

The plasticity model proposed by Keralavarma (2017) is based on a multi-surface yield criterion, obtained from the combination of the Gurson (1977) criterion and the void coalescence criterion of Keralavarma and Chockalingam (2016). The basic premise of the model is that yielding of a porous RVE at the micro-scale can occur either by diffuse plasticity of the matrix or by plastic flow localization in a band connecting neighboring voids, as illustrated schematically in Fig. 7. Yielding by diffuse plastic flow in the matrix generally prevails at dilute porosities, and is governed by the Gurson (1977) yield criterion

$$\mathcal{F}^G(\boldsymbol{\Sigma}) := \frac{\Sigma_{eq}^2}{\bar{\sigma}^2} + 2f \cosh\left(\frac{3}{2} \frac{\Sigma_m}{\bar{\sigma}}\right) - 1 - f^2 = 0 \quad (19)$$

where  $\boldsymbol{\Sigma}$  is the macroscopic stress tensor, corresponding to the average value of the Cauchy stress tensor over a micro-scale RVE defined in Eq. (6),  $\bar{\sigma}$  denotes the average or effective flow stress of the matrix material and  $f$  denotes the porosity. On the other hand, the criterion for yielding of the RVE by plastic flow localization (or coalescence) along a planar band of normal  $\underline{n}$  must be a function of the normal and shear stresses on the coalescence plane,  $\Sigma_n$  and  $\Sigma_{sh}$ , respectively, given by

$$\Sigma_n = \underline{n} \cdot \boldsymbol{\Sigma} \underline{n}, \quad \Sigma_{sh} = \sqrt{\underline{n} \cdot \boldsymbol{\Sigma}^2 \underline{n} - \Sigma_n^2}, \quad \boldsymbol{\Sigma}^2 := \boldsymbol{\Sigma} \cdot \boldsymbol{\Sigma} \quad (20)$$

Using limit analysis of a hollow cylindrical RVE containing a coaxial truncated cylindrical void, and a trial deformation field corresponding to plastic flow localization in the transverse plane of the RVE within a band of width  $W$  equal to the height of the void, Keralavarma and Chockalingam (2016) proposed the following coalescence criterion

$$\mathcal{F}^C(\boldsymbol{\Sigma}, \underline{n}) := 3 \frac{\Sigma_{sh}^2}{\bar{\sigma}^2} + 2f_b \cosh\left(\beta \frac{\Sigma_n}{\bar{\sigma}}\right) - 1 - f_b^2 = 0 \quad (21)$$

where  $f_b$  denotes the porosity of the material within the coalescence band and  $\beta$  is a parameter that depends on  $f_b$ , given by

$$\beta = \sqrt{\frac{5}{6}} \log\left(\frac{1}{f_b}\right) \left[ \sqrt{b^2 + 1} - \sqrt{b^2 + f_b^2} + b \log\left(\frac{b + \sqrt{b^2 + f_b^2}}{f_b(b + \sqrt{b^2 + 1})}\right) \right]^{-1} \quad (22)$$

and

$$b = \sqrt{\frac{1}{3} + \frac{5}{288} \frac{1}{f_b} (1 + f_b - 5f_b^2 + 3f_b^3)} \quad (23)$$

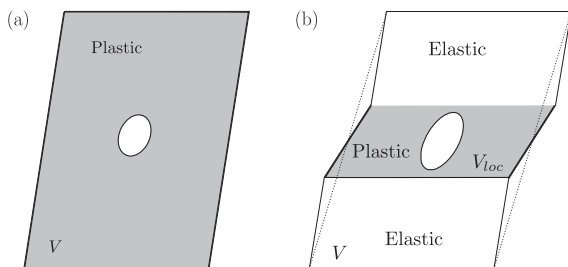


Fig. 7. Schematic diagram depicting yield of an RVE by (a) diffuse plasticity in the matrix and (b) localized plasticity in the inter-void ligaments.

The relation between  $f_b$  and the overall porosity  $f$  depends on the void shape and the geometry of the RVE. Assuming a cylindrical RVE of aspect ratio  $\alpha = c/a$ , equal to the aspect ratio of the tetragonal RVE used in the cell model simulations, and an equiaxed void shape, we obtain  $f_b = (\alpha f)^{2/3}$ .

In a statistically isotropic material containing a random distribution of equiaxed voids, the orientation of the coalescence band, defined by the unit vector  $\underline{n}$ , is determined solely by the applied state of stress. Using the multi-surface approach, one can obtain an effective isotropic coalescence domain in stress space as the region at the intersection of all coalescence domains corresponding to all possible orientations of the unit vector  $\underline{n}$  in Euclidean space. For a given state of stress  $\boldsymbol{\Sigma}$ , the value of the isotropic coalescence function,  $\mathcal{F}^{Ciso}(\boldsymbol{\Sigma})$ , can then be determined as the maximum of  $\mathcal{F}^C(\boldsymbol{\Sigma}, \underline{n})$  over all possible unit vectors  $\underline{n}$ . Thus,

$$\mathcal{F}^{Ciso}(\boldsymbol{\Sigma}) := \max_{\underline{n} \in \mathcal{U}} \mathcal{F}^C(\boldsymbol{\Sigma}, \underline{n}), \quad \mathcal{U} = \{ \underline{n} \in \mathbb{R}^3 | \underline{n} \cdot \underline{n} = 1 \} \quad (24)$$

As shown in Keralavarma (2017), the unit vector  $\underline{n}^c$  that maximizes the value of  $\mathcal{F}^C$  for a given  $\boldsymbol{\Sigma}$  must be an eigenvector of  $\boldsymbol{\Sigma}$ , or a linear combination of two eigenvectors corresponding to unequal eigenvalues. In other words, the normal to the plane of coalescence in a statistically isotropic material must fall on a principal plane of stress. If the solution  $\underline{n}^c$  coincides with a principal direction of  $\boldsymbol{\Sigma}$ , the shear stress on the plane of the coalescence band vanishes, and coalescence occurs by internal necking between neighboring voids. Otherwise,  $\underline{n}^c$  can be written as a linear combination of two eigenvectors, say  $\hat{e}_1$  and  $\hat{e}_3$ , corresponding to unequal principal stresses  $\Sigma_1 > \Sigma_3$ ; i.e.  $\underline{n}^c = \cos \phi \hat{e}_1 + \sin \phi \hat{e}_3$ . The angle  $\phi$  between  $\underline{n}^c$  and the major stress direction  $\hat{e}_1$  is determined from the condition that the normal stress on the coalescence plane  $\Sigma_n = \underline{n}^c \cdot \boldsymbol{\Sigma} \underline{n}^c$  must satisfy the transcendental equation

$$\frac{\Sigma_n}{\bar{\sigma}} - \frac{1}{3} \beta f_b \sinh\left(\beta \frac{\Sigma_n}{\bar{\sigma}}\right) = \frac{\Sigma_1 + \Sigma_3}{2\bar{\sigma}} \quad \Sigma_n \in (\Sigma_3, \Sigma_1) \quad (25)$$

If a solution exists for  $\Sigma_n$  in the range  $(\Sigma_3, \Sigma_1)$ , coalescence can occur by a combination of necking and shear localization on the above plane  $\underline{n}^c$ . Other potential solutions for  $\underline{n}^c$  can be found by considering other pairs of principal stresses and directions in (25). The isotropic coalescence function,  $\mathcal{F}^{Ciso}(\boldsymbol{\Sigma})$  defined in (24), is therefore evaluated as the maximum value of  $\mathcal{F}^C(\boldsymbol{\Sigma}, \underline{n}^c)$  over the discrete set of potential orientations of  $\underline{n}^c$  discussed above.

At small porosities, yielding generally occurs by diffuse plasticity in the matrix according to criterion (19). However, as the porosity increases due to void growth, void coalescence by strain localization becomes increasingly feasible. The competition between the two modes is captured by again using the multi-surface approach to define the overall yield domain as the region at the intersection of the Gurson and the isotropic coalescence domains. The effective isotropic yield function is then given by

$$\mathcal{F}(\boldsymbol{\Sigma}) := \max \left\{ \mathcal{F}^G(\boldsymbol{\Sigma}), \mathcal{F}^{Ciso}(\boldsymbol{\Sigma}) \right\} \quad (26)$$

where  $\mathcal{F}^G(\boldsymbol{\Sigma})$  and  $\mathcal{F}^{Ciso}(\boldsymbol{\Sigma})$  are given by (19) and (24), respectively. The above multi-surface yield function predicts a non-smooth yield surface in stress space composed of flat and curved regions and sharp corners at the intersection between different yield surfaces. Comparisons with quasi-exact yield loci obtained using a numerical limit analysis procedure in Keralavarma (2017) showed that the multi-surface criterion is more accurate than the Gurson model, particularly for large values of the porosity and/or shear dominated loading paths; although the numerical yield surfaces showed blunt corners where the multi-surface model predicted sharp ones.

### 3.2. Flow-rule and evolution of the internal variables

The macroscopic deformation rate tensor  $\mathbf{D}$  is additively decomposed into elastic and plastic parts,  $\mathbf{D} = \mathbf{D}^e + \mathbf{D}^p$ , where the elastic strain rate  $\mathbf{D}^e$  is linearly related to the Jaumann rate of the macroscopic stress using a hypoelastic constitutive law

$$\overset{\nabla}{\boldsymbol{\Sigma}} = \mathbb{C} : \mathbf{D}^e \quad (27)$$

Assuming dilute porosities, the effect of the porosity on the elastic constants is neglected, so that the stiffness tensor  $\mathbb{C}$  is assumed to be the same as for the matrix material. The macroscopic plastic deformation rate  $\mathbf{D}^p$  is obtained using the normality flow rule

$$\mathbf{D}^p = \dot{\Lambda} \mathbf{N}, \quad \mathbf{N} = \frac{\partial \mathcal{F}}{\partial \boldsymbol{\Sigma}}(\boldsymbol{\Sigma}) \quad (28)$$

where  $\dot{\Lambda} \geq 0$  denotes the macroscopic plastic multiplier, whose value is determined using the consistency condition  $\dot{\Lambda} \dot{\mathcal{F}} = 0$  for a rate independent material. The expression for the flow direction tensor  $\mathbf{N}$  depends on the active yield surface,  $\mathcal{F} = \mathcal{F}^G$  or  $\mathcal{F}^C$ . We have,

$$\mathbf{N} = \begin{cases} \mathbf{N}^G := 3 \frac{\boldsymbol{\Sigma}'}{\bar{\sigma}^2} + \frac{f}{\bar{\sigma}} \sinh\left(\frac{3}{2} \frac{\boldsymbol{\Sigma}_m}{\bar{\sigma}}\right) \mathbf{I}, & \mathcal{F} = \mathcal{F}^G \\ \mathbf{N}^C := \frac{3}{\bar{\sigma}^2} [\underline{n}^c \otimes \boldsymbol{\Sigma}_n^c + \boldsymbol{\Sigma}_n^c \otimes \underline{n}^c - 2 \boldsymbol{\Sigma}_n^c \otimes \underline{n}^c] \\ \quad + \frac{2\beta f_b}{\bar{\sigma}} \sinh\left(\beta \frac{\boldsymbol{\Sigma}_n}{\bar{\sigma}}\right) \underline{n}^c \otimes \underline{n}^c, & \mathcal{F} = \mathcal{F}^C \end{cases} \quad (29)$$

where  $\underline{n}^c$  is the unit normal vector and  $\boldsymbol{\Sigma}_n = \underline{n}^c \cdot \boldsymbol{\Sigma}_n^c$  is the normal stress on the plane of coalescence as determined earlier. Note that the normal to the yield surface is indeterminate at a yield surface corner such as  $\mathcal{F}^G = \mathcal{F}^C = 0$ , which corresponds to the onset of coalescence when both the Gurson and a coalescence criterion are satisfied simultaneously. At a yield vertex, stability of plastic flow requires that the flow direction tensor  $\mathbf{N}$  must be bounded by the normals to the two yield surfaces  $\mathbf{N}^G$  and  $\mathbf{N}^C$ . In such cases, we assume  $\mathbf{N} = \mathbf{N}^C$ , which amounts to choosing the coalescence mode of deformation at the transition from void growth to coalescence. It is observed that the above choice generally leads to the lowest rate of dissipation compared to other choices such as  $\mathbf{N} = \mathbf{N}^G$  or a conical combination of  $\mathbf{N}^G$  and  $\mathbf{N}^C$ .

The rate of evolution of porosity is proportional to the trace of  $\mathbf{D}^p$  due to plastic incompressibility of the matrix, which yields

$$\dot{f} = \begin{cases} \dot{\Lambda} (1-f) \frac{3f}{\bar{\sigma}} \sinh\left(\frac{3}{2} \frac{\boldsymbol{\Sigma}_m}{\bar{\sigma}}\right), & \mathcal{F} = \mathcal{F}^G \\ \dot{\Lambda} (1-f) \frac{2\beta f_b}{\bar{\sigma}} \sinh\left(\beta \frac{\boldsymbol{\Sigma}_n}{\bar{\sigma}}\right), & \mathcal{F} = \mathcal{F}^C \end{cases} \quad (30)$$

Analogous to the behavior of the matrix material in the cell model simulations, the macroscopic flow stress  $\bar{\sigma}$  can be written as a power law function of an average plastic arc length parameter,  $\bar{\epsilon}_{eq}^p$ , for a micro-scale RVE, as

$$\bar{\sigma} = \sigma_0 \left(1 + \frac{\bar{\epsilon}_{eq}^p}{\epsilon_0}\right)^n \quad (31)$$

where the values of the hardening parameters are assumed to be same as for the matrix material. The evolution of  $\bar{\epsilon}_{eq}^p$  is usually determined by invoking equivalence of the energy dissipation between the macroscopic material and a micro-scale RVE, which leads to the condition

$$\dot{\Lambda} \boldsymbol{\Sigma} : \mathbf{N} = (1-f) \bar{\sigma} \dot{\bar{\epsilon}}_{eq}^p \quad (32)$$

However, the above equation assumes that the dissipation is distributed throughout the matrix volume, whereas during void coalescence the deformation is localized into a band containing the void, whose volume is much smaller than the total volume of the matrix. This implies that plastic flow and strain hardening ceases in the material outside the band, while the material inside the band undergoes significantly higher plastic strains and hardening than the average given by the above equation. The volume fraction of the matrix inside the localization band equals  $\rho - f$ , where  $\rho$  is the volume fraction of the localization band. Assuming that the width  $W$  of the band scales with the size of the voids, one can write  $\rho = kf^{1/3}$ , where the value of constant  $k$  depends on the RVE geometry. If  $W$  is assumed to be equal to the height of the void normal to the band,  $k = 1$  for a random isotropic distribution of voids and  $k = \alpha^{-2/3}$  for a periodic distribution represented by the tetragonal RVE of aspect ratio  $\alpha$  in Fig. 1(b). Therefore, the condition for the equivalence of plastic dissipation at the micro- and macro-scales is amended as

$$\dot{\Lambda} \boldsymbol{\Sigma} : \mathbf{N} = \begin{cases} (1-f) \bar{\sigma} \dot{\bar{\epsilon}}_{eq}^p & \mathcal{F} = \mathcal{F}^G \\ (kf^{1/3} - f) \bar{\sigma} \dot{\bar{\epsilon}}_{eq}^p & \mathcal{F} = \mathcal{F}^C \end{cases} \quad (33)$$

from which the evolution of  $\bar{\epsilon}_{eq}^p$  is determined. Comparison with cell model simulations shows that the above modified evolution law for  $\bar{\epsilon}_{eq}^p$  is in better agreement with the numerical data than Eq. (32) for a strain hardening material, although the difference disappears as the matrix behavior approaches ideal plasticity, as expected. Further, for a hardening matrix, the best results for the effective hardening rate in the post-coalescence regime are obtained by assuming  $k = 1$ , corresponding to a cubic or random distribution of voids, irrespective of the value of  $\alpha$ . Therefore, Eq. (33) will be used with  $k = 1$  to compute the evolution of  $\bar{\epsilon}_{eq}^p$  in all the comparison results presented in the next section.

## 4. Comparison of model predictions with cell model simulations

### 4.1. Nearly ideal plastic matrix with $n = 0.01$

The yield criteria used in the multi-surface model, described in Section 3.1, have been derived using limit analysis theory, assuming ideal plastic behavior of the matrix. Strain hardening is introduced *a posteriori* using the phenomenological approach described in Section 3.2, Eq. (33). Therefore, the model predictions are first compared against cell model simulations for a power-law hardening material with a very small value of the hardening exponent,  $n = 0.01$ , whose behavior approximates that of an ideal plastic matrix.

The plasticity model presented in Section 3 is integrated under proportional loading paths for a macroscopic material point, and the predicted effective stress-strain and porosity growth response is compared with the results of cell model simulations for a periodic tetragonal lattice of voids with aspect ratio  $\alpha = 2$ . The strains to coalescence in the cell model simulations are determined as the value of the macroscopic equivalent strain to the onset of coalescence  $E_{eq}^c$  determined using the criterion  $\xi = 10$ ; see Section 2.2. These are compared with the values of the macroscopic equivalent strains at which the transition from void growth to void coalescence occurs in the continuum simulations; also denoted  $E_{eq}^c$  for simplicity. Note that, for shear dominated loading paths with  $L \approx 0$ , the multi-surface model predicts yielding to occur by localized plasticity in the inter-void ligaments, i.e.  $\mathcal{F}(\boldsymbol{\Sigma}) = \mathcal{F}^{ciso}(\boldsymbol{\Sigma})$ , at zero plastic strain (see Keralavarma, 2017); which is a consequence of the assumption of ideal plasticity in the derivation of the macroscopic yield criterion. However, it is observed in the simulations that the presence of even small amounts of strain hardening has a

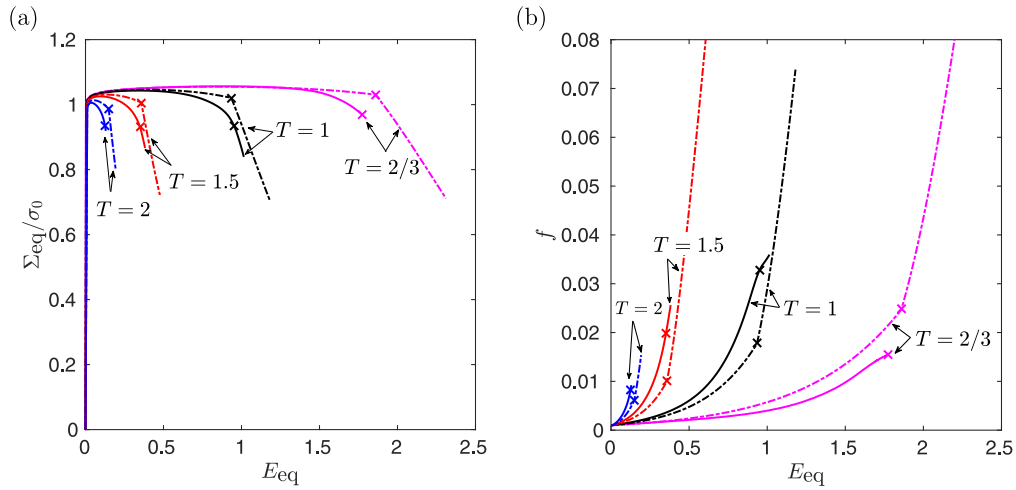


**Fig. 8.** Effective response of a tetragonal RVE with aspect ratio  $\alpha = 2$  subjected to proportional stressing with  $L = 1$  and varying  $T$ : (a) normalized equivalent stress  $\Sigma_{eq}$  vs. equivalent strain  $E_{eq}$ , (b) porosity  $f$  vs  $E_{eq}$ . Solid lines show the results of the cell model simulations, while the dashed lines show predictions from the multi-surface model. The  $\times$  marks indicate the onset of coalescence.

stabilizing effect on plastic flow, such that the material reverts to diffuse plastic flow soon after yielding occurs. Therefore, strains to coalescence  $E_{eq}^c$  reported in the continuum simulations correspond to the value of  $E_{eq}$  at which the final transition to coalescence occurs; i.e. when the stabilizing effect of strain hardening in the ligaments according to Eq. (33) is no longer sufficient to counteract the destabilizing effect of sustaining void coalescence at the micro-scale.

Fig. 8 shows the comparison of the equivalent stress strain and porosity curves for several values of the stress triaxiality and a fixed value of the Lode parameter  $L = 1$ , corresponding to axisymmetric loading with major lateral stress ( $\Sigma_1 = \Sigma_2 > \Sigma_3$ ; see Fig. 2). The equivalent stress-strain response is shown in Fig. 8(a) and the evolution of porosity  $f$  as a function of  $E_{eq}$  is shown in Fig. 8(b). The equivalent stress is shown normalized by the initial yield stress  $\sigma_0$  of the matrix. The solid lines show the average response obtained from the cell model simulations, while the dashed lines show the predictions using the multi-surface model. The  $\times$  marks indicate the onset of strain localization inside the RVE according to the criterion  $\xi = 10$  in the cell model simulations, and the onset of void coalescence in the continuum simulations, respectively. A rapid decrease in ductility with increase in  $T$  is evident, which has been well characterized in several cell model studies in the literature. Notice that the strains to coalescence predicted by the multi-surface model are in good quantitative agreement the cell model simulations.

Although the equivalent stress–strain and porosity growth response predicted by the model matches the cell model simulations at small strains, the cell model simulations show accelerated damage growth and rapid softening prior to the onset of coalescence, which is not observed in the continuum simulations. In fact, the transition from void growth to coalescence is smooth in the cell model simulations, while the model predicts an abrupt transition marked by a sharp change in slope of the curves at the onset of coalescence. This is a consequence of the multi-surface nature of the model, which results in a sharp change in the direction of plastic flow at a yield surface corner corresponding to the transition from void growth to coalescence. The comparatively smooth transition in the cell model simulations indicates that such vertices are absent in the true yield loci, as has also been observed in earlier numerical studies (Morin et al., 2016; Keralavarma, 2017). Consequently, the multi-surface model also predicts significantly lower values of the porosity  $f$  at the onset of coalescence than the

cell model, although the porosity is subsequently seen to “catch up” with the cell model simulations due to rapid post-coalescence damage growth predicted by the multi-surface model.

The porosity at the onset of coalescence obtained from the cell model simulations is seen to increase with decreasing  $T$  till  $T = 1$ , followed by a decrease for  $T = 2/3$ , although the model predicts a monotonic increase with decreasing  $T$ . Further examination shows that, the cell model simulations for  $T = 2/3$  shows a comparatively softer stress-strain response and slower damage growth rates than predicted by the model, unlike the case of  $T \geq 1$ . This is clearly an effect of induced anisotropy due to void shape evolution at low triaxialities, which is not accounted for in the isotropic multi-surface model. Hence, the comparisons between the multi-surface model and cell model simulations in the present study is restricted to moderate to large values of  $T \geq 2/3$ . Extending the present study to low triaxialities, including the important special case of pure shear ( $T = L = 0$ ), requires consideration of void shape effects and use of anisotropic yield criteria in the multi-surface model; which is left to future research. Nevertheless, the fact that the porosity at the onset of coalescence obtained from the cell model simulations varies as a function of  $T$  (and possibly also  $L$ ) shows that failure criteria based on the attainment of a critical value of the porosity, frequently used in the literature, are likely to yield poorer results than a micromechanics-based coalescence criterion used in the present study.

Fig. 9 shows similar comparison results as in Fig. 8 for a different value of  $L = 0$ , corresponding to pure shear stress states with a superposed hydrostatic stress ( $\Sigma_2 = \frac{\Sigma_1 + \Sigma_3}{2}$ ), and several values of the triaxiality  $T = 2/3, 1, 3/2$  and  $2$ . The solid lines show the results of cell model simulations while the dashed lines show predictions from the multi-surface model. It is clear from the figure that the effective strains to the onset of coalescence  $E_{eq}^c$ , marked by the  $\times$  symbols, are lower by at least an order of magnitude than for  $L = 1$ . It can be shown using a simple minimum dissipation argument that, in a periodically voided ideal plastic material subjected to pure shear, it is always energetically favorable for the strain to localize along a band of voids irrespective of the porosity, as has been recognized previously in the literature (Drucker, 1966; Leblond and Mottet, 2008). Therefore, in a very low hardening matrix with  $n = 0.01$  under predominantly shear loadings ( $|L| \ll 1$ ), strain localization occurs at very small plastic strains and nearly the initial porosity levels in the cell model simulations. The multi-surface model predicts the same trends with the variation of

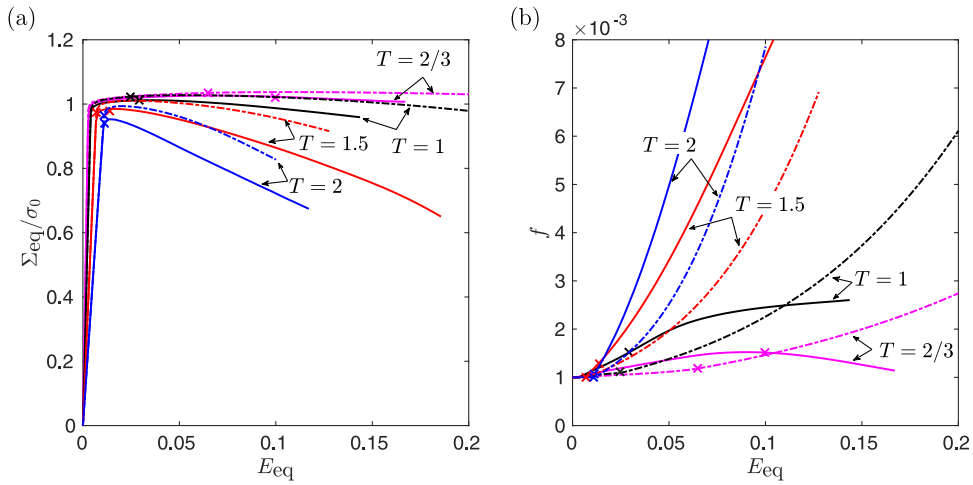


**Fig. 9.** Effective response of a tetragonal RVE with aspect ratio  $\alpha = 2$  subjected to proportional stressing with  $L = 0$  and varying  $T$ : (a) normalized equivalent stress  $\Sigma_{eq}$  vs. equivalent strain  $E_{eq}$ , (b) porosity  $f$  vs  $E_{eq}$ . Solid lines show the results of the cell model simulations, while the dashed lines show predictions from the multi-surface model. The  $\times$  marks indicate the onset of coalescence.

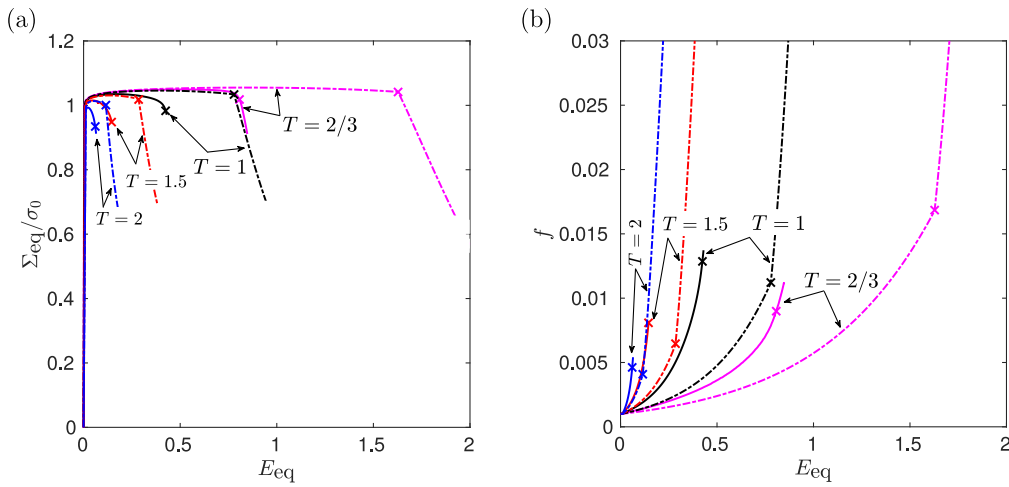


**Fig. 10.** Effective response of a tetragonal RVE with aspect ratio  $\alpha = 2$  subjected to proportional stressing with  $L = -1$  and varying  $T$ : (a) normalized equivalent stress  $\Sigma_{eq}$  vs. equivalent strain  $E_{eq}$ , (b) porosity  $f$  vs  $E_{eq}$ . Solid lines show the results of the cell model simulations, while the dashed lines show predictions from the multi-surface model. The  $\times$  marks indicate the onset of coalescence.

the equivalent strains to coalescence  $E_{eq}^c$  as a function of  $T$ , in good agreement with the cell model simulations. The porosity curves in Fig. 9(b) show that, for  $T = 1$  and  $T = 2/3$ , the behavior of the unit cells is qualitatively different from the predictions of the multi-surface model. While the model predicts a monotonic increase in  $f$  as a function of  $E_{eq}$  with the rate increasing as a function of  $T$ , the simulation for  $T = 2/3$  shows the porosity increasing till the onset of localization followed by a decrease due to void closure inside the localized shear field between neighboring voids. As discussed earlier, the multi-surface model is unable to predict such low triaxiality effects due to the assumption of isotropy.

Fig. 10 shows the comparison of the effective stress-strain and porosity growth curves for  $L = -1$ , corresponding to axisymmetric loadings with major axial stress ( $\Sigma_1 > \Sigma_2 = \Sigma_3$ ) and several values of the triaxiality. Comparison with Figs. 8 and 9 shows that, for a given value of  $T$ , the ductility observed in the cell model simulations for  $L = -1$  is smaller than for  $L = 1$ , although significantly higher than the ductility for  $L = 0$ . Moreover, unlike for  $L = 1$  and 0, the multi-surface model is seen to significantly overestimate the ductility for all values of  $T$ , although the difference is most pronounced for the lower values of  $T$ . Fig. 10(b) also shows that the multi-surface model significantly underesti-

mates the porosity growth rates for all values of  $T$ . This behavior of the Gurson model, which is identical to the multi-surface model till the onset of coalescence, is well known from the early ductile fracture studies that focused on axisymmetric stress states; and is usually corrected by the introduction of Tvergaard’s  $q$ -parameters (Tvergaard, 1982; Koplik and Needleman, 1988). However, the results of Fig. 8 shows that such correction is likely to lead to an underestimation of the ductility for loading paths close to  $L = 1$ . It is worth mentioning that the cell model simulation results in Fig. 10 are obtained for a specific orientation of the RVE corresponding to  $\phi = 45^\circ$  in Fig. 2(a), which is close to the minimum ductility orientation according to the result of Fig. 6, while most simulations in the literature consider  $\phi = 0^\circ$  corresponding to the RVE aligned with the axis of symmetry of the loading. Nevertheless, in both cases the multi-surface model can be shown to underestimate the damage growth rates and overestimate the ductility.

Cell models simulations of the type shown in Figs. 8–10 have been performed over a range of intermediate values of  $L \in [-1, 1]$  and several values of  $T \geq 2/3$ . Fig. 11 shows a comparison of the strains to coalescence  $E_{eq}^c$  obtained in the cell model simulations with those predicted by the multi-surface model for a power-law

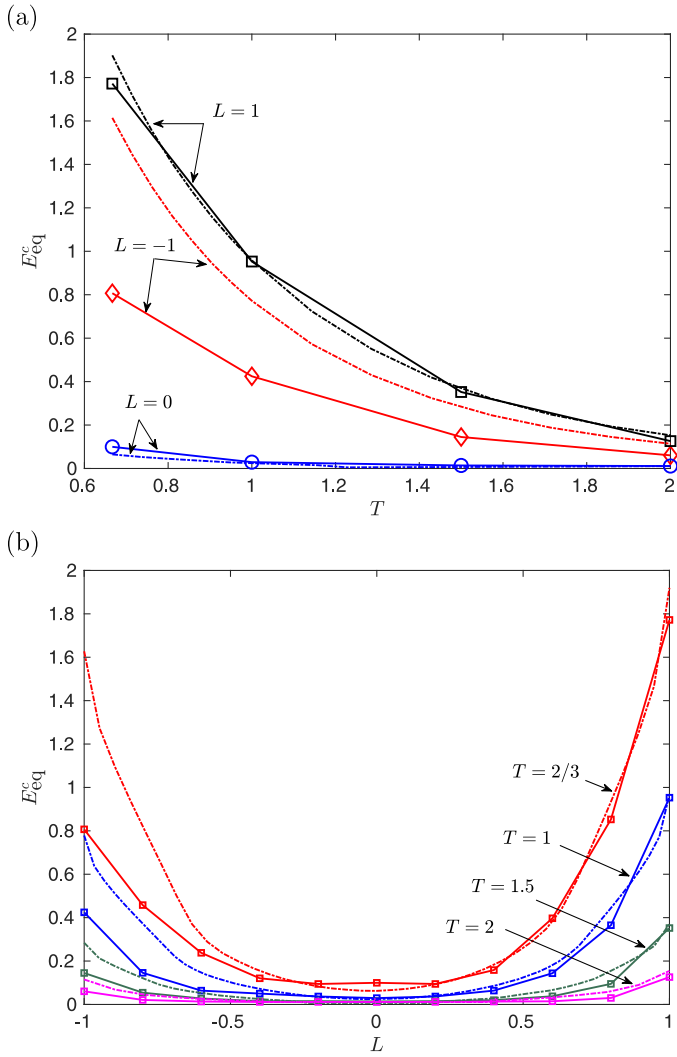


**Fig. 11.** Macroscopic equivalent strains to coalescence  $E_{eq}^c$  as a function of (a)  $T$  for various constant values of  $L$ , and (b)  $L$  for various constant values of  $T$ . The points connected by solid lines show the results of cell model simulations while the dashed lines show predictions from the multi-surface model.

hardening material with  $n = 0.01$ . The points connected by solid lines show the data from the cell model simulations, while the dashed curves show the predictions from the multi-surface model. Fig. 11(a) shows the variation of  $E_{eq}^c$  as a function of  $T$  for the three values of the Lode parameter shown in Figs. 8–10. Notice that the strains to coalescence obtained from the cell model simulations for  $L = 1$  and  $L = 0$  fall nicely on the corresponding curves predicted by the multi-surface model. For the case  $L = -1$ , the model overestimates the ductility for all  $T$  as noted in Fig. 10, although the predicted variation of  $E_{eq}^c$  with  $T$  is qualitatively similar to that obtained from the cell model simulations.

Fig. 11(b) shows the variation of the ductility as a function of  $L$  for various constant values of  $T$ . The multi-surface model predictions for  $E_{eq}^c$  are in good quantitative agreement with the cell model simulations over a wide range of values of  $L$  for  $T \geq 2/3$ . Importantly, the multi-surface model reproduces the approximately convex shapes of the failure loci and the asymmetry between positive and negative values of  $L$  at fixed  $T$ , which indicates that the transitions in the failure mechanisms as a function of the loading path are correctly captured by the model. Quantitative discrepancies are observed for loading paths near  $L = -1$  (axisymmetric loadings with major axial stress), for which the multi-surface model overestimates the ductility, as shown in Fig. 10. In

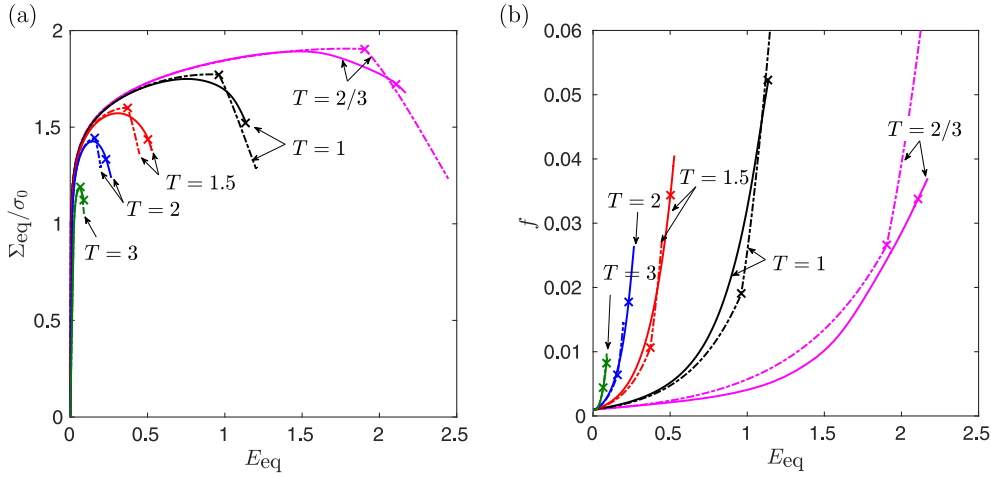
fact, the cell model simulations evidence a stronger asymmetry between positive and negative values of  $L$  or, equivalently, the sign of the determinant of the deviatoric stress, than the multi-surface model. Nevertheless, it is remarkable that the multi-surface model, in the absence of heuristic adjustable parameters, is able to achieve good quantitative comparison with the cell model simulations for proportional loading paths over a wide range of values of  $T$  and  $L$ . It is worth noting that, all the simulation results using the multi-surface model in this section used the modified evolution law for the equivalent plastic strain, Eq. (33), which has different forms in the pre- and post-coalescence stages. However, for a nearly ideal plastic matrix with  $n = 0.01$ , use of the “standard” evolution law for  $\bar{\epsilon}_{eq}^p$ , Eq. (32), leads to nearly similar results for the ductility (not shown) as in Fig. 11.

#### 4.2. Strain hardening matrix with $n = 0.1$

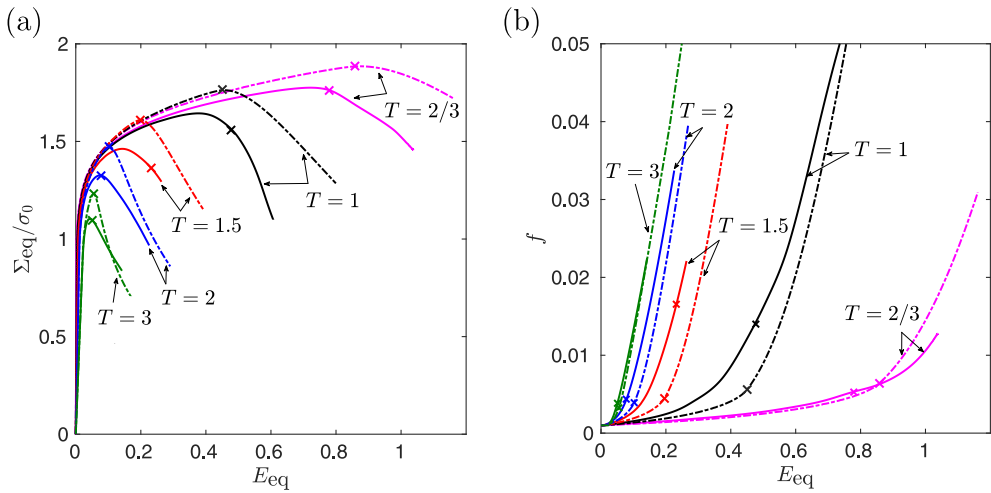
Strain hardening has the effect of stabilizing plastic flow and delaying the onset of plastic instabilities in continuum simulations. Therefore, strain hardening can also be expected to increase the intrinsic ductility of a porous material by delaying the onset of void coalescence by plastic strain localization inside a micro-scale RVE. In this section, we compare the effective response and ductility predictions obtained in the cell model simulations for a power-law hardening matrix with exponent  $n = 0.1$ , with the predictions from the multi-surface model. The chosen value of  $n$  is typical of the hardening exponent of structural metals in their annealed state.

Fig. 12 shows the comparison of the cell model simulations with the model predictions for axisymmetric loading paths with major lateral stress ( $L = 1$ ) and several values of the triaxiality. As in Figs. 8–10, the cell model results are shown using solid lines while the model predictions appear using dashed lines. Unlike for  $n = 0.01$ , the equivalent flow stress increases by a factor of 1.5–2 due to strain hardening before the ultimate stress is reached. The equivalent stress-strain curves in Fig. 12(a) show that the model predictions are in very good agreement with the cell model simulations up to the ultimate stress point. Beyond the ultimate stress point, plasticity begins to localize inside the unit cell, resulting in additional softening before the coalescence criterion is satisfied at the points marked by the  $\times$ . Note that, unlike in the cell model simulations, the transition to coalescence is abrupt in the case of the multi-surface model, corresponding to the sudden change of the plastic flow direction at a yield surface corner. Nevertheless, the predicted values of the strains to the onset of coalescence  $E_{eq}^c$  are comparable between the model and the cell model simulations. However, unlike in the case of  $n = 0.01$ , the multi-surface model is seen to slightly underestimate the ductility for all values of  $T$  shown. The comparison of the porosity curves in Fig. 12(b) are qualitatively similar to Fig. 8(b) for  $n = 0.01$ , with the model underestimating the porosity at the onset of coalescence, although the subsequent rapid growth of porosity is in good agreement with the cell model simulations.

Fig. 13 shows the comparison of the multi-surface model predictions with cell model simulations for generalized shear loadings with  $L = 0$  and several values of  $T$ . Unlike for the case of  $L = 1$ , the model predicts a transition to the coalescence branch of the yield criterion (i.e.  $\mathcal{F} = \mathcal{F}^c$ ) immediately upon yielding, due to the fact that the multi-surface model predicts a lower yield stress for localized yielding compared to diffuse yielding irrespective of the value of  $f$ . However, notice that the final transition to void coalescence occurs in the model at much higher plastic strains near the ultimate stress point, as shown using the  $\times$  marks on the dashed curves. This is a consequence of the fact that the hardening law in Eq. (33) predicts a significantly higher hardening rate when the deformation is localized between the voids, which stabilizes



**Fig. 12.** Effective response of a tetragonal RVE with aspect ratio  $\alpha = 2$  subjected to proportional stressing with  $L = 1$  and varying  $T$ : (a) normalized equivalent stress  $\Sigma_{eq}$  vs. equivalent strain  $E_{eq}$ , (b) porosity  $f$  vs  $E_{eq}$ . Solid lines show the results of the cell model simulations, while the dashed lines show predictions from the multi-surface model. The  $\times$  marks indicate the onset of coalescence.



**Fig. 13.** Effective response of a tetragonal RVE with aspect ratio  $\alpha = 2$  subjected to proportional stressing with  $L = 0$  and varying  $T$ : (a) normalized equivalent stress  $\Sigma_{eq}$  vs. equivalent strain  $E_{eq}$ , (b) porosity  $f$  vs  $E_{eq}$ . Solid lines show the results of the cell model simulations, while the dashed lines show predictions from the multi-surface model. The  $\times$  marks indicate the onset of coalescence.

plastic flow in the ligaments and leads to the model switching back to the diffuse mode of plastic flow. This behavior of the model is physical and can also be observed in some cell model simulations for shear dominated loadings, where the values of the localization indicator  $\xi$  shows low amplitude fluctuations at small strains, before coalescence occurs at much larger porosities when the hardening capacity of the material is no longer sufficient to counteract the destabilizing effect of void growth on the plastic flow. It is observed from Fig. 13 that the macroscopic strains to coalescence  $E_{eq}^c$  predicted by the model are in good quantitative agreement with the cell model simulations for all values of  $T$ . As shown in Fig. 13(b), the model underestimates the porosity at coalescence compared to the cell model simulations, although the overall porosity curves match well with the cell model simulations; i.e. the effect of  $T$  on damage growth is well predicted by the model.

Fig. 14 shows the comparison for  $L = -1$  (axisymmetric loading with major axial stress) and several values of  $T$  for a hardening material with  $n = 0.1$ . Notice that, as in the case of the low hardening material with  $n = 0.01$ , the model overestimates the ductility for low values of  $T$ . This is also reflected in the porosity growth plots, which show good quantitative agreement for  $T \geq 3/2$ ,

although the porosity at failure is underestimated by the model. However, for low values of  $T$ , the model predicts significantly lower damage growth rates and higher strains to coalescence than the cell model data. As mentioned in the context of Fig. 10, these discrepancies are correctable by the introduction of heuristics such as Tvergaard’s  $q$ -parameters, although it is *a priori* unclear what effect this will have on the failure strains predicted by the model for loading paths other than axisymmetric.

Fig. 15 summarizes the results of all the simulations done for  $n = 0.1$  by plotting the strains to coalescence  $E_{eq}^c$  as a function of  $T$  and  $L$  in Fig. 15(a) and (b), respectively. The variation of  $E_{eq}^c$  with  $T$  in Fig. 15(a) for  $L = 0$  and  $\pm 1$  shows that the model predicts the correct qualitative trends for the  $T$  and  $L$  dependence of ductility. Good quantitative agreement is observed for  $L = 0$ , although the model overestimates the ductilities for  $L = -1$  at low  $T$  and underestimates the ductilities for  $L = 1$  for all values of  $T$ . Fig. 15(b) shows that the Lode parameter dependence of ductility is correctly captured by the model for values of  $T \geq 2/3$ , along with reasonably good quantitative agreement except for axisymmetric loading paths. Note that the above comparison is achieved using the modified evolution of equation for  $\tilde{\epsilon}_{eq}^p$  in Eq. (33). Unlike for  $n = 0.01$ , using the original version (32) of the energy balance condition to

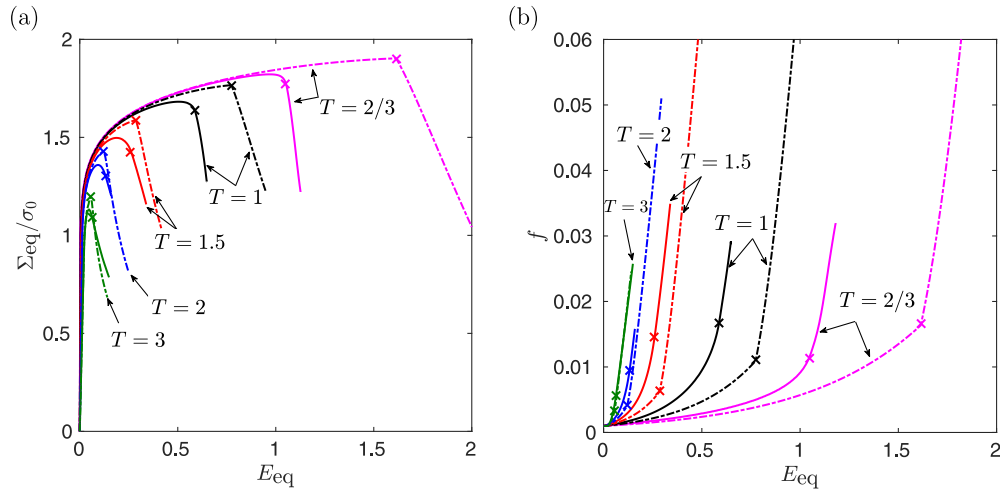


**Fig. 14.** Effective response of a tetragonal RVE with aspect ratio  $\alpha = 2$  subjected to proportional stressing with  $L = -1$  and varying  $T$ : (a) normalized equivalent stress  $\Sigma_{eq}$  vs. equivalent strain  $E_{eq}$ , (b) porosity  $f$  vs.  $E_{eq}$ . Solid lines show the results of the cell model simulations, while the dashed lines show predictions from the multi-surface model. The  $\times$  marks indicate the onset of coalescence.

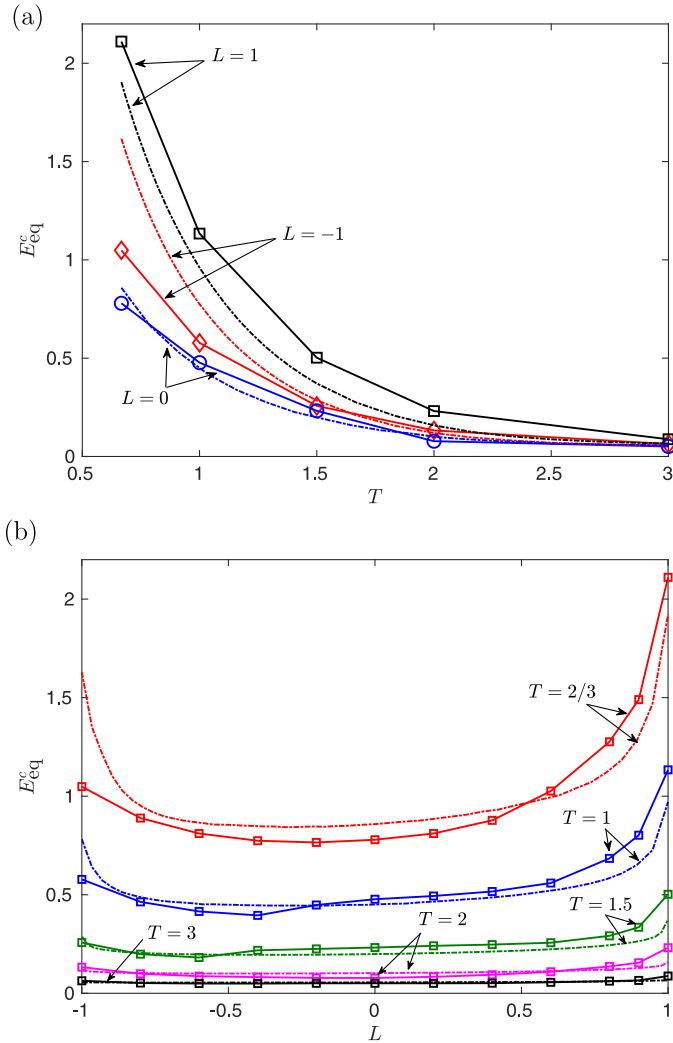


**Fig. 15.** Macroscopic equivalent strains to coalescence  $E_{eq}^c$  as a function of (a)  $T$  for various constant values of  $L$ , and (b)  $L$  for various constant values of  $T$ . The points connected by solid lines show the results of cell model simulations while the dashed lines show predictions from the multi-surface model.

compute  $\dot{\epsilon}_{eq}^p$  leads to the model significantly under-predicting the ductility compared to the cell model simulations. The corresponding plots are omitted for brevity.

Most importantly, the results in Fig. 15 indicate that the multi-surface model, sans any heuristic adjustable parameters, provides reasonably good quantitative match with the cell model simulations over a wide range of values of  $L$  and moderate to high values of  $T$ . As remarked previously, it is possible that introduction of additional heuristics in the model can potentially improve the comparison with cell model data even for axisymmetric states near  $L = \pm 1$ . However, existing approaches such as use of Tvergaard’s  $q$ -parameters achieve reduced ductility by accelerating the damage growth rates for all values of  $T$  and  $L$ , which is likely to result in a poorer comparison with the unit cell data for shear dominated loading paths. Consideration of such heuristics is outside the scope of the present paper.

**5. Discussion**

Cell model analysis of the type performed here has long been used to study the micro-mechanisms of ductile failure (Tvergaard, 1982; Koplik and Needleman, 1988); with recent work focused on understanding the influence of the third invariant of the deviatoric stress, or the Lode parameter, on the ductility under proportional loading conditions (Barsoum and Faleskog, 2011; Dunand and Mohr, 2014; Tekoglu, 2014; Luo and Gao, 2018). The trends from our cell model simulations are consistent with the results of all the above studies, with the strains to failure decreasing exponentially as a function of the stress triaxiality, and lower ductilities predicted under shear dominated loading conditions compared to axisymmetric loading paths at fixed triaxiality. Plots of the equivalent strains to failure as a function of  $L$  at fixed  $T$ , shown in Figs. 11(b) and 15(b), have approximately convex asymmetric shapes with a minimum in ductility for small negative values of  $L$ .

Widely used continuum plasticity models such as the Rice and Tracey (1969) and the Gurson–Tvergaard–Needleman (GTN) models (Tvergaard and Needleman, 1984) do not predict the Lode parameter influence on ductility, as damage growth in these models is independent of  $L$  and depends only on  $T$ . Several phenomenological extensions of the GTN model have been developed recently to account for the so called shear damage effect, starting with the works of Xue (2008) and Nahshon and Hutchinson (2008); although these models typically introduce additional

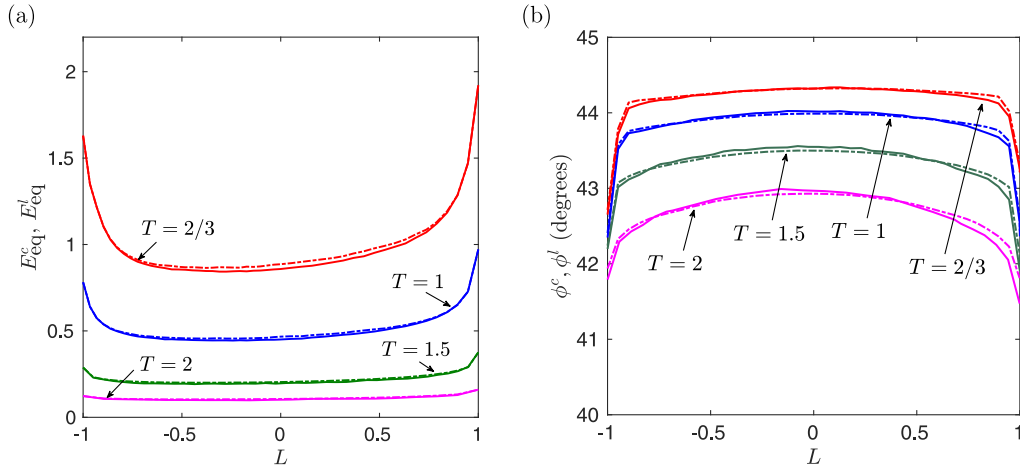


**Fig. 16.** (a) Comparison of the equivalent strains to the onset of coalescence  $E_{eq}^c$  (solid lines) and the strains to the onset of macroscopic localization according to the criterion of Rice (1976) (dashed lines), in the simulations using the multi-surface model. (b) Comparison of the model predictions for the angle between the coalescence plane normal  $\underline{n}^c$  and the major principal stress direction  $\hat{e}_1$ ,  $\phi^c$  (solid lines), and the angle between the normal to the plane on which the Rice localization criterion is satisfied  $\underline{n}^l$  and  $\hat{e}_1$ ,  $\phi^l$  (dashed lines). The hardening exponent is  $n = 0.1$ .

heuristic parameters that need to be calibrated from experimental data. To the best of our knowledge, none of the above models have been shown to quantitatively match the cell model simulation data for the Lode parameter dependence of ductility evidenced in Figs. 6, 11 and 15. It should be mentioned that uncoupled ductile damage models (in the terminology of Pineau et al., 2016) have been developed recently to account for the influence of shear on ductility at low triaxialities (Bai and Wierzbicki, 2008; Mohr and Marcadet, 2015), which can predict the  $L$  dependence of ductility observed in the experiments; albeit with the introduction of several heuristic fitting parameters.

In contrast with the above mentioned “shear modified” damage models, the multi-surface model has been developed using micromechanical analysis accounting for different possible modes of yielding within a micro-scale porous RVE. Assuming diffuse plastic flow in the RVE leads to the classical Gurson (1977) model, while the assumption of localized plasticity in the RVE leads to a void coalescence criterion that has a fundamentally different form from the Gurson criterion (Keralavarma and Chockalingam, 2016). The results of the present study show that an isotropic continuum plasticity model constructed from the combination of the Gurson criterion and the above coalescence criterion can quantitatively reproduce the loading path dependence of ductility observed in the cell model simulations, under moderate to high triaxiality loading conditions. It is further shown that, with the addition of a micromechanics-based coalescence criterion to the Gurson model, use of Tvergaard and Needleman (1984)’s heuristic parameters such as  $q_1$ ,  $q_2$ ,  $q_3$  and  $f_c$  are not necessary to obtain good comparison with the large deformation elastic-plastic behavior of porous unit cells, over a wide range of values of  $T$  and  $L$  under proportional stressing. Significant quantitative discrepancies are observed only in the case of axisymmetric loading, the correction of which possibly requires more sophisticated heuristics than in the GTN model.

In both the continuum and the cell model simulations, the ductility has been quantified as the equivalent strain till the onset of void coalescence at the microscopic scale of the voids. On the other hand, the ductility in macroscopic structures is often limited by the localization of plastic flow due to plastic instability, such as necking in round bars and shear banding in plane specimens, followed by rapid void growth and coalescence inside the localization bands. Due to the use of periodic boundary conditions in the cell model simulations, the average response of the RVE nominally represents

the behavior of a homogeneously deforming material at the macro-scale; so that such macroscopic localization phenomena cannot be captured in our study. Nevertheless, for a homogeneously deforming material, Rice (1976) (also see Rudnicki and Rice, 1975) has shown that the criterion for the nucleation of a localization band can be written in terms of the fourth order elasto-plastic tangent stiffness tensor,  $\mathbb{C}^t$ . According to Rice’s criterion, a homogeneous plastic flow field can localize into a planar band with normal  $\underline{n}^l$  when the determinant of the acoustic tensor,  $\mathbf{A}$ , defined as

$$\mathbf{A}(\underline{n}^l) = \underline{n}^l \cdot \mathbb{C}^t \cdot \underline{n}^l \quad (34)$$

vanishes. The minimum value of  $\det(\mathbf{A})$ , over all possible spatial orientations of the unit vector  $\underline{n}^l$ , is tracked in the continuum simulations using the multi-surface model in Section 4. The strain to the onset of macroscopic plastic instability according to the Rice criterion,  $E_{eq}^l$ , is determined as the smallest value of  $E_{eq}$  at which  $\det(\mathbf{A}) \leq 0$  for any direction  $\underline{n}^l$ .

Fig. 16(a) shows a comparison of the strains to the onset of coalescence  $E_{eq}^c$ , and macroscopic plastic instability  $E_{eq}^l$  predicted by the Rice criterion, as a function of  $L$  for four different values of  $T$ . The results shown correspond to a strain hardening matrix with  $n = 0.1$ , although similar results (not shown) are also obtained for  $n = 0.01$ . Notice that, for all values of  $T$  and  $L$ , the value of  $E_{eq}^l$  is equal to or greater than the value of  $E_{eq}^c$ . Further, the curves for  $E_{eq}^c$  and  $E_{eq}^l$  vs.  $L$  are close to each other, indicating that the onset of macroscopic instability is predicted soon after the onset of void coalescence at the micro-scale. This result appears to suggest that a change in the mechanism of yielding at the micro-scale (i.e. the onset of void coalescence in the present case) can act as a potential trigger for the onset of plastic instabilities at the macro-scale; a hypothesis that has been put forth earlier by Rice (1976). In order to verify this hypothesis, we examine the correlation between the orientation of the plane  $\underline{n}^l$  for which the Rice instability criterion is first satisfied, with the orientation of the plane  $\underline{n}^c$  on which void coalescence is predicted at the micro-scale in the continuum simulations. Fig. 16(b) plots the angles  $\phi^l$  and  $\phi^c$  that the vectors  $\underline{n}^l$  and  $\underline{n}^c$ , respectively, makes with the major loading direction  $\hat{e}_1$ , as a function of  $L$  for several values of  $T$ . It is clear from the figure that the two angles nearly coincide and, more importantly, exhibit identical trends for the variation with  $L$  and  $T$ . This result indicates that, not only can the onset of macro-scale localization lead to void growth and coalescence at the micro-scale, the converse is also possible where the onset of coalescence at the

micro-scale can act as a trigger for the onset of plastic instabilities at the macro-scale. Hence, it seems reasonable to expect that in materials containing a non-uniform distribution of defects or under non-homogeneous loading conditions, the onset of void coalescence locally due to excessive damage growth or stress concentrations can trigger the onset of macroscopic instabilities such as shear bands.

It is emphasized that the results in Fig. 16 are obtained under the assumption of proportional loading up to and beyond the onset of coalescence at the micro-scale; which is difficult to reproduce in laboratory experiments. In reality, the onset of macroscopic localization is almost always accompanied by a change of constraint for the material within the localization band, which will have a significant impact on the ductility obtained in fracture experiments. A typical example is the increase in stress triaxiality experienced by the material in the minimum section of a necked tensile specimen, which leads to rapid acceleration of the damage growth inside the neck. While our simulation approach does not allow for such loading path changes resulting from the onset of macro-scale localization, more sophisticated approaches have been used to capture this effect in cell model studies (Tekoğlu et al., 2015). Notably, Tekoğlu et al. (2015)'s study shows that the onset of void coalescence often occurs after the onset of macroscopic localization, unlike in Fig. 16; although the two phenomena occur at nearly identical values of the macroscopic equivalent strain. Therefore, the use of a sophisticated plasticity model such as the multi-surface model that can predict the loading path dependence of damage growth and material softening can be expected to lead to more accurate prediction of the onset of plastic instability, and consequently the ductility, in structural simulations.

Perhaps the most significant limitation of the multi-surface model is the assumption of isotropy, which restricts its domain of applicability to moderate to large values of the triaxiality. This is evident from the comparison of the model predictions with cell model simulation results for  $T = 2/3$ , which shows greater discrepancies with the model predictions than for higher values of  $T$ . Significantly, the cell model simulations for  $T = 2/3$  predicted both softer stress-strain behavior and slower void growth rates than predicted by the model, which clearly indicates that anisotropy due to void shape evolution has an important effect on the response for this value of  $T$ . In fact, it is known from prior cell model studies under axisymmetric conditions that negligible void growth occurs for values of  $T \leq 1/3$  (Benzerga and Leblond, 2010); so that the porosity can no longer be used as a useful measure of damage, and void shape effects must be considered. Nevertheless, the isotropic multi-surface model can be shown to be an improvement over the widely used GTN model in ductile fracture simulations involving the growth of a dominant crack, such as the tensile failure of a round smooth and notched bars (Reddi et al., 2019).

On the other hand, parameter-free prediction of ductile failure by shear band instability under low triaxiality (typically  $T \leq 1/3$ ) loadings probably requires the use anisotropic models, many of which have been developed in recent years (Monchiet et al., 2008; Keralavarma and Benzerga, 2008; 2010; Madou and Leblond, 2012a; 2012b). These anisotropic models have been shown to reproduce several experimental features of ductile failure under low triaxiality shear dominated loading conditions (Morin et al., 2017; Torki and Benzerga, 2018), or in the presence of strong textural anisotropies (Benzerga et al., 2019). It is possible to extend the multi-surface approach of Keralavarma (2017) for an anisotropic ductile material by combining an anisotropic void growth criterion, including void shape and material anisotropy effects such as Keralavarma and Benzerga (2010), with the coalescence criterion of Keralavarma and Chockalingam (2016). The resulting model can be expected to capture the anisotropic effects on void growth and coalescence under low triaxiality loading conditions. Such models

are currently under development and will be reported in future publications.

## 6. Conclusion

Periodic cell model simulations of void growth to coalescence in an elasto-plastic power law hardening material under proportional loading have been performed to study the loading path dependence of ductile failure. The results of the cell model simulations are compared against predictions from an isotropic continuum plasticity model, based on a multi-surface yield criterion that accounts for void growth by diffuse plastic flow as well as void coalescence along a band of voids. It is shown that the multi-surface model, in the absence of heuristic adjustable parameters, is able to quantitatively match the strains to failure obtained from the cell model simulations, over a wide range of values of the Lode parameter and moderate to large triaxialities. Additional conclusions from the study are listed below.

- The cell model simulations predict that the equivalent strain to the onset of coalescence,  $E_{eq}^c$ , is an exponentially decreasing function of  $T$ , and an approximately convex non-monotonic function of  $L$  at fixed  $T$ . Minimum ductility is predicted for shear dominated loadings with  $L < 0$  at constant  $T$ , in agreement with the results of recent three dimensional cell model studies.
- Motivated by the physics of void coalescence inside a micro-scale RVE, a new phenomenological hardening law has been proposed for continuum simulations using the multi-surface model.
- The multi-surface model predictions for the equivalent strains to the onset of void coalescence  $E_{eq}^c$  are shown to be in good quantitative agreement with the values of  $E_{eq}^c$  obtained from the cell model simulations, for both nearly ideal plastic matrix behavior (hardening exponent  $n = 0.01$ ) and a hardening matrix ( $n = 0.1$ ).
- The largest discrepancies between the model predictions with cell model simulations are observed for axisymmetric loading paths with  $L = \pm 1$  and for the lowest value of the triaxiality  $T = 2/3$  considered. It is concluded that the latter is a result of void shape effects playing an increasingly important role at low triaxialities, which is not accounted for in the isotropic model.

## Acknowledgements

We thank the anonymous reviewer, whose comments have resulted in significant improvements to the manuscript.

## Appendix A. Periodic boundary conditions for the unit cell

Periodic boundary conditions are imposed on the RVE shown in Fig. 2(a) using multi-point constraint equations relating the relevant degrees of freedom of periodic image nodes; using a method previously employed in Tekoğlu (2014) (also see Barsoum and Faleskog, 2011; Dunand and Mohr, 2014). Let  $D_i$  ( $i = 1..3$ ) denote the length of the RVE in the  $\mathbf{e}_i$  direction in the reference configuration; i.e.  $D_1 = D_3 = a$  and  $D_2 = c$ . Cartesian components of the position vector of a point,  $\mathbf{X}$ , in the reference configuration are denoted by  $X_i$ .

On the right and left boundaries with normals  $\pm \mathbf{e}_1$  ( $X_1 = \pm D_1/2$ ):

$$\begin{aligned} u_1(D_1/2, X_2, X_3) - u_1(-D_1/2, X_2, X_3) &= 2U_1 \\ u_2(D_1/2, X_2, X_3) - u_2(-D_1/2, X_2, X_3) &= 0 \\ u_3(D_1/2, X_2, X_3) - u_3(-D_1/2, X_2, X_3) &= 0 \end{aligned} \quad (\text{A.1})$$

On the top boundary with normal  $\underline{e}_2$  ( $X_2 = D_2/2$ ):

$$\begin{aligned} u_1(+X_1, D_2/2, X_3) + u_1(-X_1, D_2/2, X_3) &= 2U_T \\ u_2(+X_1, D_2/2, X_3) + u_2(-X_1, D_2/2, X_3) &= 2U_2 \\ u_3(+X_1, D_2/2, X_3) - u_3(-X_1, D_2/2, X_3) &= 0 \end{aligned} \quad (\text{A.2})$$

On the bottom boundary with normal  $-\underline{e}_2$  ( $X_2 = 0$ ):

$$\begin{aligned} u_1(+X_1, 0, X_3) + u_1(-X_1, 0, X_3) &= 0 \\ u_2(+X_1, 0, X_3) + u_2(-X_1, 0, X_3) &= 0 \\ u_3(+X_1, 0, X_3) - u_3(-X_1, 0, X_3) &= 0 \end{aligned} \quad (\text{A.3})$$

On the front and back faces with normals  $\pm \underline{e}_3$  ( $X_3 = 0$  and  $-D_3/2$  respectively):

$$\begin{aligned} u_3(X_1, X_2, 0) &= 0 \\ u_3(X_1, X_2, -D_3/2) &= -U_3 \end{aligned} \quad (\text{A.4})$$

## Appendix B. Components of the normalized stress tensor $\mathbf{S}(\mathbf{T}, \mathbf{L}, \phi)$

The components of  $\mathbf{S} = \Sigma/\Sigma_{\text{eq}}$  in the principal coordinate system of  $\Sigma$  ( $\hat{\underline{e}}_1, \hat{\underline{e}}_2, \hat{\underline{e}}_3$ ) can be written as

$$[\hat{\mathbf{S}}] = \begin{bmatrix} S_1 & 0 & 0 \\ 0 & S_2 & 0 \\ 0 & 0 & S_3 \end{bmatrix} \quad (\text{B.1})$$

where

$$\begin{aligned} S_1 &= T + \frac{2}{3} \cos \theta, \quad S_2 = T - \frac{2}{3} \cos \left( \theta + \frac{\pi}{3} \right), \\ S_3 &= T - \frac{2}{3} \cos \left( \theta - \frac{\pi}{3} \right) \end{aligned} \quad (\text{B.2})$$

and  $\theta \in [0, \frac{\pi}{3}]$  is the Lode angle defined by  $\theta = \frac{1}{3} \cos^{-1}(-L)$ . The principal directions are ordered such that the condition  $S_1 \geq S_2 \geq S_3$  is satisfied. If  $T \geq 1/6$ , the maximum principal stress also equals the absolute maximum normal stress. The eigenvectors of  $\Sigma$  can be written in terms of the base vectors of the principal coordinate system of the RVE ( $\underline{e}_1, \underline{e}_2, \underline{e}_3$ ) as (see Fig. 2)

$$\hat{\underline{e}}_1 = -\sin \phi \underline{e}_1 + \cos \phi \underline{e}_2, \quad \hat{\underline{e}}_2 = \underline{e}_3, \quad \hat{\underline{e}}_3 = \cos \phi \underline{e}_1 + \sin \phi \underline{e}_2 \quad (\text{B.3})$$

where  $\phi$  is the angle between the  $c$ -axis of the tetragonal RVE and the major principal direction  $\hat{\underline{e}}_1$ . Using the appropriate coordinate transformation, the components of  $\mathbf{S}$  in the ( $\underline{e}_1, \underline{e}_2, \underline{e}_3$ ) frame are

$$[\mathbf{S}] = \begin{bmatrix} S_{11} & S_{12} & 0 \\ S_{12} & S_{22} & 0 \\ 0 & 0 & S_{33} \end{bmatrix} \quad (\text{B.4})$$

where

$$\begin{aligned} S_{11} &= T + \frac{2}{3} \cos \theta - \left( \cos \theta + \frac{1}{\sqrt{3}} \sin \theta \right) \cos^2 \phi \\ S_{22} &= T - \frac{2}{3} \cos \left( \theta - \frac{\pi}{3} \right) + \frac{2}{3} \left( \cos \theta + \cos \left( \theta - \frac{\pi}{3} \right) \right) \cos^2 \phi \\ S_{33} &= T - \frac{2}{3} \cos \left( \theta + \frac{\pi}{3} \right) \\ S_{12} &= -\frac{1}{2} \left( \cos \theta + \frac{1}{\sqrt{3}} \sin \theta \right) \sin 2\phi \end{aligned} \quad (\text{B.5})$$

## References

Bai, Y., Wierzbicki, T., 2008. A new model of metal plasticity and fracture with pressure and lode dependence. *Int. J. Plast.* 24 (6), 1071–1096.  
 Bao, Y., Wierzbicki, T., 2004. On fracture locus in the equivalent strain and stress triaxiality space. *Int. J. of Mech. Sci.* 46 (81), 81–98.

Barsoum, I., Faleskog, J., 2007. Rupture mechanisms in combined tension and shear-experiments. *Int. J. Solids Struct.* 44, 1768–1786.  
 Barsoum, I., Faleskog, J., 2011. Micromechanical analysis on the influence of the lode parameter on void growth and coalescence. *Int. J. Solids Struct.* 48 (6), 925–938.  
 Benzerga, A.A., 2002. Micromechanics of coalescence in ductile fracture. *J. Mech. Phys. Solids* 50, 1331–1362.  
 Benzerga, A.A., Besson, J., 2001. Plastic potentials for anisotropic porous solids. *Eur. J. Mech.* 20 (3), 397–434.  
 Benzerga, A.A., Leblond, J.B., 2010. Ductile fracture by void growth to coalescence. *Adv. Appl. Mech.* 44, 169–305.  
 Benzerga, A.A., Leblond, J.B., 2014. Effective yield criterion accounting for microvoid coalescence. *J. App. Mech.* 81, 031009.  
 Benzerga, A.A., Surovik, D., Keralavarma, S.M., 2012. On the path-dependence of the fracture locus in ductile materials—analysis. *Int. J. Plast.* 37, 157–170.  
 Benzerga, A.A., Thomas, N., Herrington, J.S., 2019. Plastic flow anisotropy drives shear fracture. *Sci. Rep.* 9 (1), 1425.  
 Danas, K., Ponte Castañeda, P., 2009. A finite-strain model for anisotropic viscoplastic porous media: I—theory. *Eur. J. Mech./A Solids* 28, 387–401.  
 Danas, K., Ponte Castañeda, P., 2009. A finite-strain model for anisotropic viscoplastic porous media: II—applications. *Eur. J. Mech./A Solids* 28, 402–416.  
 Danas, K., Ponte Castañeda, P., 2012. Influence of the lode parameter and the stress triaxiality on the failure of elasto-plastic porous materials. *Int. J. Solids Struct.* 49 (11), 1325–1342.  
 Drucker, D.C., 1966. Continuum theory of plasticity on macroscale and microscale. *J. Mater.* 1 (4), 873.  
 Dunand, M., Mohr, D., 2011. On the predictive capabilities of the shear modified Gurson and the modified Mohr–Coulomb fracture models over a wide range of stress triaxialities and lode angles. *J. Mech. Phys. Solids* 59, 1374–1394.  
 Dunand, M., Mohr, D., 2014. Effect of lode parameter on plastic flow localization after proportional loading at low stress triaxialities. *J. Mech. Phys. Solids* 66, 133–153.  
 Gologanu, M., Leblond, J.B., Devaux, J., 1993. Approximate models for ductile metals containing non-spherical voids – case of axisymmetric prolate ellipsoidal cavities. *J. Mech. Phys. Solids* 41 (11), 1723–1754.  
 Gologanu, M., Leblond, J.B., Perrin, G., Devaux, J., 1997. Recent extensions of Gurson's model for porous ductile metals. In: Suquet, P. (Ed.), *Continuum Micromechanics*, CISM Lectures Series. Springer, New York, pp. 61–130.  
 Gurson, A.L., 1977. Continuum theory of ductile rupture by void nucleation and growth: part I—yield criteria and flow rules for porous ductile media. *J. Eng. Mat. Tech.* 99, 2–15.  
 Haltom, S.S., Kyriakides, S., Ravi-Chandar, K., 2013. Ductile failure under combined shear and tension. *Int. J. Solids Struct.* 50 (10), 1507–1522.  
 Hancock, J.W., Brown, D.K., 1983. On the role of strain and stress state in ductile failure. *J. Mech. Phys. Solids* 31, 1–24.  
 Hancock, J.W., MacKenzie, A.C., 1976. On the mechanisms of ductile failure in high-strength steels subjected to multi-axial stress states. *J. Mech. Phys. Solids* 24, 147–169.  
 Idiart, M., Ponte Castañeda, P., 2005. Second-order estimates for nonlinear isotropic composites with spherical pores and rigid particles. *C. R. Mecanique* 333, 147–154.  
 Johnson, G.R., Cook, W.H., 1985. Fracture characteristics of three metals subjected to various strains, strain rates, temperatures and pressures. *Eng. Fract. Mech.* 21 (1), 31–48.  
 Kailasam, M., Castañeda, P., 1998. A general constitutive theory for linear and nonlinear particulate media with microstructure evolution. *J. Mech. Phys. Solids* 46 (3), 427–465.  
 Keralavarma, S.M., 2017. A multi-surface plasticity model for ductile fracture simulations. *J. Mech. Phys. Solids* 103, 100–120.  
 Keralavarma, S.M., Benzerga, A.A., 2008. An approximate yield criterion for anisotropic porous media. *C. R. Mecanique* 336, 685–692.  
 Keralavarma, S.M., Benzerga, A.A., 2010. A constitutive model for plastically anisotropic solids with non-spherical voids. *J. Mech. Phys. Solids* 58, 874–901.  
 Keralavarma, S.M., Chockalingam, S., 2016. A criterion for void coalescence in anisotropic ductile materials. *Int. J. Plast.* 82, 159–176.  
 Koplik, J., Needleman, A., 1988. Void growth and coalescence in porous plastic solids. *Int. J. Solids Struct.* 24 (8), 835–853.  
 Leblond, J.B., Mottet, G., 2008. A theoretical approach of strain localization within thin planar bands in porous ductile materials. *C. R. Mecanique* 336, 176–189.  
 Luo, T., Gao, X., 2018. On the prediction of ductile fracture by void coalescence and strain localization. *J. Mech. Phys. Solids* 113, 82–104.  
 Madou, K., Leblond, J.B., 2012a. A Gurson-type criterion for porous ductile solids containing arbitrary ellipsoidal voids—I: limit-analysis of some representative cell. *J. Mech. Phys. Solids* 60, 1020–1036.  
 Madou, K., Leblond, J.B., 2012. A Gurson-type criterion for porous ductile solids containing arbitrary ellipsoidal voids—II: determination of yield criterion parameters. *J. Mech. Phys. Solids* 60, 1037–1058.  
 Mohr, D., Marcadet, S.J., 2015. Micromechanically-motivated phenomenological Hosford–Coulomb model for predicting ductile fracture initiation at low stress triaxialities. *Int. J. Solids Struct.* 67, 40–55.  
 Monchiet, V., Cazacu, O., Charkaluk, E., Kondo, D., 2008. Macroscopic yield criteria for plastic anisotropic materials containing spheroidal voids. *Int. J. Plast.* 24, 1158–1189.  
 Morin, L., Leblond, J.B., Benzerga, A.A., 2015. Coalescence of voids by internal necking: theoretical estimates and numerical results. *J. Mech. Phys. Solids* 75, 140–158.

- Morin, L., Leblond, J.B., Benzerga, A.A., Kondo, D., 2016. A unified criterion for the growth and coalescence of microvoids. *J. Mech. Phys. Solids* 97, 19–36.
- Morin, L., Leblond, J.B., Mohr, D., Kondo, D., 2017. Prediction of shear-dominated ductile fracture in a butterfly specimen using a model of plastic porous solids including void shape effects. *Eur. J. Mech. A/Solids* 61, 433–442.
- Nahshon, K., Hutchinson, J.W., 2008. Modification of the Gurson model for shear failure. *Eur. J. Mech.* 27, 1–17.
- Needleman, A., Tvergaard, V., 1992. Analyses of plastic flow localization in metals. *Appl. Mech. Rev.* 45, S3–S18.
- Nielsen, K.L., Dahl, J., Tvergaard, V., 2012. Collapse and coalescence of spherical voids subject to intense shearing: studied in full 3d. *Int. J. Fract.* 177, 97–108.
- Papasidero, J., Doquet, V., Mohr, D., 2015. Ductile fracture of aluminum 2024-t351 under proportional and non-proportional multi-axial loading: Bao-Wierzbicki results revisited. *Int. J. Solids Struct.* 69, 459–474.
- Pardoën, T., Hutchinson, J.W., 2000. An extended model for void growth and coalescence. *J. Mech. Phys. Solids* 48, 2467–2512.
- Pineau, A., Benzerga, A.A., Pardoën, T., 2016. Failure of metals I: brittle and ductile fracture. *Acta Mater.* 107, 424–483.
- Reddi, D., Areej, V.K., Keralavarma, S.M., 2019. Ductile failure simulations using a multi-surface coupled damage-plasticity model. *Int. J. Plast.* doi:10.1016/j.ijplas.2019.02.007.
- Rice, J., 1976. The localization of plastic deformation. In: Koiter, W. (Ed.), *Proceedings of the Fourteenth International Congress of Theoretical and Applied Mechanics*. North-Holland, Amsterdam, pp. 207–220.
- Rice, J.R., Tracey, D.M., 1969. On the enlargement of voids in triaxial stress fields. *J. Mech. Phys. Solids* 17, 201–217.
- Rudnicki, J.W., Rice, J.R., 1975. Conditions for the localization of deformation in pressure-sensitive dilatant materials. *J. Mech. Phys. Solids* 23, 371–394.
- Tekoglu, C., 2014. Representative volume element calculations under constant stress triaxiality, lode parameter, and shear ratio. *Int. J. Solids Struct.* 51 (25–26), 4544–4553.
- Tekoglu, C., Leblond, J.B., Pardoën, T., 2012. A criterion for the onset of void coalescence under combined tension and shear. *J. Mech. Phys. Solids* 60, 1363–1381.
- Tekoğlu, C., Hutchinson, J.W., Pardoën, T., 2015. On localization and void coalescence as a precursor to ductile fracture. *Philos. Trans. R. Soc. Lond. A Math. Phys. Eng. Sci.* 373, 20140121.
- Thomas, N., Basu, S., Benzerga, A.A., 2016. On fracture loci of ductile materials under non-proportional loading. *Int. J. Mech. Sci.* 117, 135–151.
- Thomason, P.F., 1985. A three-dimensional model for ductile fracture by the growth and coalescence of microvoids. *Acta Metall.* 33 (6), 1087–1095.
- Torki, M.E., Benzerga, A.A., 2018. A mechanism of failure in shear bands. *Extrem. Mech. Lett.* 23, 67–71.
- Torki, M.E., Benzerga, A.A., Leblond, J.B., 2015. On void coalescence under combined tension and shear. *J. App. Mech.* 82, 071005.
- Tvergaard, V., 1981. Influence of voids on shear band instabilities under plane strain conditions. *Int. J. Fract.* 17, 389–407.
- Tvergaard, V., 1982. On localization in ductile materials containing spherical voids. *Int. J. Fract.* 18, 237–252.
- Tvergaard, V., Needleman, A., 1984. Analysis of the cup-cone fracture in a round tensile bar. *Acta Metall.* 32, 157–169.
- Xue, L., 2007. Damage accumulation and fracture initiation in uncracked ductile solids subject to triaxial loading. *Int. J. Solids Struct.* 44, 5163–5181.
- Xue, L., 2008. Constitutive modeling of void shearing effect in ductile fracture of porous materials. *Eng. Fract. Mech.* 75, 3343–3366.
- Zhu, Y., Engelhardt, M.D., Kiran, R., 2018. Combined effects of triaxiality, lode parameter and shear stress on void growth and coalescence. *Eng. Fract. Mech.* 199, 410–437.